Title

Enzyme expression kinetics by Escherichia coli during transition from rich to minimal media depends on proteome reserves.

Journal

Nature Microbiology, 8(2)

Authors

Wu, Chenhao
Okano, Hiroyuki
Aebersold, Ruedi
et al.

Publication Date

2023-02-01

DOI

10.1038/s41564-022-01310-w

Peer reviewed

Published in final edited form as:

Nat Microbiol. 2023 February ; 8(2): 347–359. doi:10.1038/s41564-022-01310-w.

Enzyme expression kinetics by *Escherichia coli* during transition from rich to minimal media depends on proteome reserves

Chenhao Wu[1,*,†], **Matteo Mori**[1,†], **Miriam Abele**[2,3], **Amir Banaei-Esfahani**[4], **Zhongge Zhang**[5], **Hiroyuki Okano**[1], **Ruedi Aebersold**[4,6], **Christina Ludwig**[2,*], **Terence Hwa**[1,5,*]

[1]Department of Physics, U.C. San Diego, La Jolla, CA 92093-0319

[2]Bavarian Center for Biomolecular Mass Spectrometry, Technical University of Munich, Freising, Germany

[3]Chair of Proteomics and Bioanalytics, Technical University of Munich, Freising, Germany

[4]Department of Biology, Institute of Molecular Systems Biology, ETH, Zurich, Switzerland

[5]Division of Biological Sciences, U.C. San Diego, La Jolla, CA 92093

[6]Faculty of Science, University of Zurich, Zurich, Switzerland

Abstract

Bacterial fitness depends on adaptability to changing environments. In rich growth medium, which is replete with amino acids, *Escherichia coli* primarily expresses protein synthesis machineries, which comprise ~40% of cellular proteins, and are required for rapid growth. Upon transition to minimal medium, which lacks amino acids, biosynthetic enzymes are synthesized, eventually reaching ~15% of cellular proteins when growth fully resumes. We applied quantitative proteomics to analyze the timing of enzyme expression during such transitions, and established a simple positive relation between the onset time of enzyme synthesis and the fractional enzyme "reserve" maintained by *E. coli* while growing in rich media. We devised and validated a coarse-grained kinetic model that quantitatively captures the enzyme recovery kinetics in different pathways, based solely on the proteomes immediately preceding the transition and well after its completion. Our model enables us to infer regulatory strategies underlying the "as needed" gene-expression program adopted by *E. coli*.

In the wild, bacteria are exposed to rapidly changing nutrient environments, including feast-like conditions with abundant amino acids and saccharides such as those in the mammalian gut soon after meals (1, 2), and famine-like conditions as what enteric bacteria

[*]corresponding authors: Chenhao Wu (tierwuchen@gmail.com), Christina Ludwig (tina.ludwig@tum.de), Terence Hwa (thwa@ucsd.edu).

[†]These authors contributed equally to this work.

Author Contribution Statement

C.W. and T.H. designed the experimental and theoretical studies. C.W. performed most of the measurements other than proteomics, with contributions from H.O. and Z.Z; M.A. and A. B.-E. performed proteomic experiments with supervision from R.A. and C.L.; C.W. and M.M. performed the quantitative modeling and theoretical analysis; M.M. developed the improved xTop2.0 algorithm and performed quantitative analysis of proteomic data. All authors contributed to the writing of the manuscript.

Competing interests Statement

The authors declare no competing interests.

encounter when they are released into the sewar (3, 4). Rapid adaptation by bacteria to the changing environment is crucial for bacteria to seize opportunities to proliferate as much as possible given the nutrients available, and to cope and survive when nutrients are depleted (5, 6). Early studies of bacterial adaptation to nutrient environment were done during steady state growth, and discovered the differential allocation of the bacterial proteome to ribosomes, organized in accordance to the growth rate (7-9). More recent studies found orderly adjustment of the bacterial proteome in other components of the proteome besides the ribosomes (10-14). Focusing on bacteria growing on minimal medium, with a spectrum of growth rates obtained by using different carbon sources, by chemostat set to different dilution rates, or with growth reduction set by various sublethal doses of antibiotics, proteomic methods have been used to quantify and predict how the bacterial proteome is allocated into various functional groups (15-19) and during transitions from one carbon source to another (11, 20-23). During the course of these studies, theoretical models have been developed to explain growth phenotypes, including the quantitative prediction of lag times for different transitions based on only steady state data (24-29). However, most of the quantitative studies have so far been limited to bacteria in minimal medium with defined (and simple) carbon and nitrogen sources. Much less is known at the quantitative level for bacterial growth in different ‘rich media’ containing a multitude of amino acids and other nutrients, even though such nutrient conditions may be more common in natural habitats (e.g., the gut for enteric bacteria (1, 2) than minimal medium, at least until substrates present in rich media are exhausted.

In order to fill in the knowledge gap on proteome allocation for bacteria in rich media, we characterized the proteome of *E. coli* cells grown in a variety of ‘rich media’ commonly used in laboratory studies, with the full supplement of amino acids, with/without nucleotides and vitamins, and with/without the additional supplement of a carbon source. We focused on the dynamics during growth transition from rich to minimal media, particularly the kinetics of the onset of various biosynthetic pathways that are needed for growth in minimal media but not in rich media. Our study relied on DIA-based quantitative mass-spectrometry proteomics (19) along with an improved protein quantification method (xTop v2.0), which allowed us to estimate errors in the protein abundances from the available peptide precursor signals.

Results

Proteome allocation during growth in rich and minimal media

We characterized the proteomes of exponentially growing *E. coli* K-12 cells in four common ‘rich media’ using a recently developed protein quantification method (19). Accurate, quantitative measurements of protein abundances were obtained by data independent acquisition (DIA) mass spectrometry followed with library-based (30, 31) and library-free (directDIA) data analysis approaches. Protein abundances were inferred from peptide measurements using the recently developed algorithm xTop (19). Here, we further extended the analysis by developing a framework to estimating the uncertainty in the measured abundances, crucial for comparison of results across growth conditions or over a time series as will be done below. Our uncertainty estimate leverages the Bayesian framework

upon which the xTop algorithm is built to calculate condition- and protein-specific uncertainties arising from the scatter in peptide precursors (Supplementary Note 1). We combined relative quantification provided by this updated xTop v2.0 algorithm with absolute quantification provided by ribosome profiling (32), to yield accurate protein abundances and associated uncertainties for about 2000 proteins in each condition (Methods). For the ease of comparison to previous studies on proteome allocation in minimal media, we also characterized the proteomes of the same cells growing in MOPS-based minimal medium with glucose as the sole carbon source, as well as for cells subjected to reduced glucose uptake as characterized previously (15, 19, 32).

Fig. 1a shows the growth rate of wild-type cells in various rich and minimal glucose media; see Supplementary Table 1, 2 for the medium composition used and strain details. As expected, the addition of casamino acid (CAA, containing amino acid monomers) or rich-defined medium (RDM, containing amino acids, nucleotides, and vitamins (33)) to glucose minimal medium increased the steady-state growth rate. Interestingly however, while the growth on CAA alone well exceeded that on glucose alone, further addition of glucose boosted the growth more than the addition of nucleotides and vitamins (RDM alone). This underscores the dominant roles amino acids and additional carbon supplies play in rapid bacterial growth, with the supply of nucleotides and vitamins exerting relatively minor effects.

The total abundances of expressed proteins in several main functional groups (defined in Supplementary Table 3 based on pathways described in Refs. (34, 35)) are shown in Fig. 1b for wild type cells grown in glucose minimal medium and in glucose supplemented by RDM. Here and throughout the text, the abundance of a protein i is reported as the mass fraction of that protein among the total cellular protein mass, denoted as ϕ_i, and the abundance of a functional group is the sum of the mass fraction of all proteins in that group. Fig. 1a shows the clear dominance of translation-related proteins for growth in rich medium and the co-dominance of translation-related proteins and amino-acid biosynthesis (AAB) enzymes in minimal medium. By plotting the abundance of translation-related proteins against the growth rate of each culture, we found a linear increase, by ~14%-proteome from glucose alone to glucose supplemented with RDM (Fig. 1c), with similar increases for ribosomal proteins and auxiliary proteins including elongation factors and tRNA synthetases (Extended Data Fig. 1a-c). Since translational elongation rate is nearly saturated in these growth conditions (36), the observed increase in the abundance of translational machinery reflects what is needed to increase protein synthesis flux in rich media, as already reported for bacterial physiology (8, 10, 37, 38).

The total cellular protein content increases with cell volume for cells grown in different media (19, 39-41), so the abundance measured in mass fraction is approximately proportional to the cellular protein concentration, with mass fraction of 1% corresponding to $\sim 5 \times 10^4$ proteins per μm^3 of cell volume for typical proteins 250aa in length (41). Thus, the increased concentration of translational proteins in rich media is necessarily accompanied by decreased concentrations of other proteins. We found that this decrease was mainly achieved by reductions in AAB enzymes, from ~15% to < 4% of total protein mass when

supplied with either CAA or RDM (Fig. 1d); similar reallocation has also been reported in *S. cerevisiae* (42). The role of nucleotide synthesis in proteome allocation is negligible in comparison since the changes are below 1%-proteome (Fig. 1e). The TCA cycle was reduced with RDM supplement by ~2%-proteome (Fig. 1g); but this was largely offset by the increase in allocation for fermentation to acetate (Fig. 1f).

Next, we compare the proteome of cells grown in CAA or RDM, with and without glucose supplement. The boost of 20-30% in growth rate due to glucose supplementation, which required a ~5%-proteome increase in translational proteins (Fig. 1c), is accompanied with reduced allocation for enzymes of TCA cycle (2.5%-proteome), glycolysis/gluconeogenesis, fermentation to acetate, and ATPase (~0.5%-proteome each); compare open and filled green symbols in Fig. 1f-i. The reallocation pattern we observed suggests that enzymes additionally required for growth in rich medium, in the absence of a supplemental carbon source, are mainly those involved in energy biogenesis and the biosynthesis of other non-AA carbon components (e.g., lipids and cell-wall component) from one or more amino acids (AA); see detailed examination in Extended Data Fig. 2.

Growth lag during amino acid downshift

We found that the reallocation of the proteome from AA biosynthesis to translational machineries is a primary requirement for cells to grow fast in rich media (Fig. 1). However, removal of AAB enzymes from the proteome makes it more difficult for cells to maintain growth once the supply of AA is exhausted, because *de novo* AA biosynthesis is needed (Fig. 2a). This could result in a lag in growth recovery when cells are shifted from rich to minimal media.

To analyse the anticipated growth-lag, we grew cells in media with all 20 AAs (Supplementary Table 4) supplemented by glucose, and shifted mid-exponential cultures to the same medium containing glucose but lacking AAs (Fig. 2b; Methods). A 2-hour lag was observed before growth recovery (Extended Data Fig. 3a, 3b). For convenience, most of our subsequent experiments used a mix of 18 AAs, with two minor AAs, cysteine and tyrosine, excluded due to their instability (cysteine) and poor solubility (tyrosine). The kinetics of growth recovery without these two minor AAs is indistinguishable from that with all 20 AAs (Extended Data Fig. 3b).

We hypothesized that the lag might arise due to bottlenecks in *de novo* AA biosynthesis and carbon substrate uptake. We first tested the effect of different carbon supplements on AA downshift kinetics. Carbon substrates that enter central metabolism from upper glycolysis (Supplementary Table 5) all had lag times of ~2h (Fig. 2c) despite differences in their pre- and post-shift growth rates (Fig. 2d, 2e). To test whether the uptake of glycolytic carbon sources is strongly repressed before downshifts, we performed AA downshift with glycerol, whose uptake system is well characterized (43): Repeating the AA downshift experiment with glycerol with a mutant *E. co*li (NQ399, Supplementary Table 1) that has glycerol uptake proteins GlpFK strongly expressed (11), we observed the same 2h lag (Extended Data Fig. 3c-d). We concluded that the 2h lag arises from internal growth bottleneck(s) related to abrupt AA removal when shifting from rich to minimal media. Next, we investigated the 2h lag for the downshift from 18AA to none using glycerol as the carbon

supplement [hereafter used as a standard downshift protocol and just referred to as “AA downshift” for simplicity]. The steady-state mass fractions of the main protein groups in the pre-shift condition of this standard AA downshift (Extended Data Fig. 1d-k) were consistent with those in other rich conditions.

Proteomic analysis during AA downshift

To quantitate cellular recovery kinetics, we analysed the proteome after AA downshift using mass spectrometry-based proteomics (19). Extended Data Fig. 4 (up-triangles) show two biological replicates of the time courses of the protein functional groups, with the instantaneous growth rate plotted in Extended Data Fig. 4l for reference. The group of AAB enzymes increased the most (~8%-proteome) during the shift (Extended Data Fig. 4b). Interestingly, glycerol uptake enzymes increased too (Extended Data Fig. 4k), even though glycerol uptake was not a bottleneck (Extended Data Fig. 3d).

The protein mass fractions plotted in Extended Data Fig. 4 were derived by summing up mass fractions of individual proteins from each group. In Extended Data Fig. 4b much larger protein changes of some individual AAB enzymes are masked by the summing process. Individual AAB enzymes are shown in Extended Data Fig. 5, grouped according to pathways. (Due to the excellent repeatability of the results shown in Extended Data Fig. 4, here we only show the data for set 1.) The responses exhibited across these pathways were quite diverse, both in terms of fold changes and recovery kinetics: MetE showed >100-fold change (Extended Data Fig. 5a) while enzymes in threonine synthesis pathway showed no more than two-fold change (Extended Data Fig. 5j). Some enzymes started increasing their abundances in the early stage of the shift, e.g., the methionine and arginine pathways (Extended Data Fig. 5a,b), while other enzymes did not increase until 100 min after the shift, e.g., the serine and threonine pathways (Extended Data Fig. 5i, j).

As the enzymes in the same pathway had similar kinetics, attributed in part to operon structure (indicated in Extended Data Fig. 5), we summed up the abundances of enzymes in the same pathway to obtain a finer grained view of the kinetic response of the AAB enzymes in Fig. 3a, which identified a variety of fold-changes (y-axis) and onset times (x-axis). The inverse of the fold-change, which is the pre-expression level of a pathway relative to its final expression level (for steady state growth in glycerol minimal medium), referred to as (fractional) “pre-shift reserve”, is plotted in increasing order in Fig. 3b. The plot reveals a surprising exponential separation of the pre-shift reserves as indicated by the red dashed line.

The kinetic behaviors of the AAB enzymes for the first several groups are plotted in order in panels Fig. 3c through Fig. 3k, with the remainders and replicates shown in Extended Data Fig. 6. A systematic change in recovery kinetics was observed in Fig. 3c-3k, with the enzyme groups with the smaller pre-shift reserve responding earlier after the shift. To further quantitate recovery kinetics, we estimated the recovery onset time of each group; see Extended Data Fig. 7a. Plotting the onset time obtained against the reciprocal of the fold change, we obtained a smoothly increasing relation (triangles, Fig. 3l). This relation obtained is robust to the precise definition of the onset time (Extended Data Fig. 7b-g), and is moreover seen not only at the pathway level, but also for individual AAB enzymes

(blue triangles in Fig. 3m). Correlations between onset time and the pre- and post- shift abundances themselves, or their differences, are much weaker (Extended Data Fig. 7h-m). Our data thus reveals a simple rule, that the recovery onset time of AAB enzymes is an increasing function of the fractional pre-shift reserves.

Modelling AA downshift kinetics

The correlation between enzyme onset time and pre-shift reserve is reminiscent of qualitative predictions made in a theoretical study by Pavlov and Ehrenberg (PE) (44), who proposed that allocating protein synthesis preferentially to enzyme groups with the smallest reserve would provide the fastest recovery. However, it is difficult to obtain concrete predictions on enzyme onset times from the PE model in order to compare to the data, since the PE model was assumed to be globally applicable to all enzymes, while the relationship observed between onset time and pre-shift reserve was specific for AAB enzymes, but not for the majority of other detected proteins (circles vs. triangles, Fig. 3m). We incorporated elements of the PE model into a coarse-grained model of flux-controlled proteome allocation (21) to quantitate the onset of AAB enzymes, and their effect on the overall growth recovery.

Qualitatively, the problem cells face right after AA downshift can be described as follows: Cells need to make AAB enzymes to supply the missing AA influx. However, the overall protein synthesis flux is limited due to the lack of AAs. Therefore, it is necessary to reallocate the limited protein synthesis flux towards AAB enzymes right after the shift, away from the synthesis of ribosomal proteins which dominated before the shift (Fig. 2a). The generic kinetic equations for the j^{th} AAB enzyme group (of proteomic mass fraction $\phi_{A,j}(t)$) and ribosomal proteins (of mass fraction $\phi_{Rb}(t)$) can be written as (Supplementary Note 2)

$$\frac{d\phi_{A,j}}{dt} = \lambda(t) \cdot \left(\chi_{A,j}(t) - \phi_{A,j}(t)\right), \tag{1}$$

$$\frac{d\phi_{Rb}}{dt} = \lambda(t) \cdot \left(\chi_{Rb}(t) - \phi_{Rb}(t)\right). \tag{2}$$

Here $\lambda(t) \equiv \frac{d}{dt} \ln M(t)$ is the instantaneous growth rate during the shift, with $M(t)$ being the total protein mass at time t after shift. It describes the magnitude of protein synthesis flux ($dM\ /\ dt$) normalized by the total protein mass. $\chi_{A,j}(t)$ and $\chi_{Rb}(t)$ are "allocation functions" describing the fraction of protein synthesis flux directed towards synthesizing the j^{th} AAB enzyme group and ribosomal proteins, respectively. In order to solve the recovery kinetics, it is necessary to specify the time dependence of growth rate $\lambda(t)$ and the allocation functions $\chi_{A,j}(t)$, $\chi_{Rb}(t)$ in terms of the dynamical variables, $\phi_{A,j}(t)$, $\phi_{Rb}(t)$.

We adopted the PE model (44), setting the instantaneous growth rate in terms of the abundances of the rate-limiting enzyme group(s), in this case, the AAB enzyme groups $\phi_{A,j}(t)$, as

$$\frac{\lambda(t)}{\lambda^*} = \min_j \left(\frac{\phi_{A,j}(t)}{\phi^*_{A,j}} \right) = \min_j q_j(t)\,. \tag{3}$$

Here λ^* and $\phi^*_{A,j}$ represent the growth rate and the abundance of the j^{th} AAB enzyme group in the post-shift steady-state, respectively, and $q_j(t) \equiv \phi_{A,j}(t) \,/\, \phi^*_{A,j}$ is the enzyme abundance relative to the final abundance, i.e., the fractional enzyme reserve. As elaborated in Supplementary Note 2B, Eq. (3) is simply a statement that the protein synthesis flux (proportional to $\lambda(t)$) is governed by the abundance of the most bottlenecked enzyme group(s), a result which follows from the assumption that the catalytic rates of the growth-limiting enzyme groups are at maximum (i.e., uninhibited) as are the catalytic rates in the post-shift steady-state, with allosteric inhibition of the non-limiting AAB enzymes (45).

Specifying the time-dependent allocation functions $\chi_{A,j}(t)$, $\chi_{Rb}(t)$ involves more effort. Molecularly, the synthesis of different enzyme groups are regulated by their corresponding AA products (Fig. 4a). According to the well-known mechanisms of end-products inhibition (45, 46), the synthesis of growth-limiting AAB enzyme group(s) are expected to be up-regulated due to the low concentration of their AA products, while synthesis of non-growth limiting group(s) are expected to be repressed due to the accumulation of their corresponding AA products. To determine the protein synthesis flux allocated to each AAB group without requiring molecular details (which are mostly unknown at the quantitative level), we developed a two-stage allocation scheme as illustrated in Fig. 4a: In the first stage, we extended the scheme of flux-controlled regulation (FCR) introduced by Erickson et al (21) and reviewed in (14) to describe the allocation between ribosome synthesis $\chi_{Rb}(t)$ and *total* AAB enzyme synthesis $\chi_{A,tot}(t)$, which is based molecularly on ppGpp-mediated regulation (47). Then in the second stage, we describe more refined sub-allocation of the AAB enzymes to each group, i.e., from $\chi_{A,tot}(t)$ to $\chi_{A,j}(t)$, which is based on end-product inhibition.

In the FCR scheme, the translational activity, defined as

$$\sigma(t) \equiv \lambda(t) \,/\, \phi_{Rb}(t), \tag{4}$$

is taken to represent the overall abundance of the AA pools while growth is limited by AA synthesis (Eq. (3)). Using $\sigma(t)$, we can express the allocation functions $\chi_{A,tot}(t)$ and $\chi_{Rb}(t)$ in terms of the *regulatory functions* $\hat{\chi}_{A,tot}(\sigma)$ and $\hat{\chi}_{Rb}(\sigma)$, as

$$\chi_{A,tot}(t) = \hat{\chi}_{A,tot}(\sigma(t)), \tag{5}$$

$$\chi_{Rb}(t) = \hat{\chi}_{Rb}(\sigma(t))\,. \tag{6}$$

The forms of these regulatory functions, shown in Fig. 4b, can be determined from steady-state measurements as detailed in Extended Data Fig. 8. We see that under limited growth

(small σ), ribosomal synthesis is repressed while AAB enzyme synthesis is induced as may be expected intuitively. Molecularly, the translational activity $\sigma(t)$ is represented (inversely) by the ppGpp signaling system, during growth transition and in steady-state (47, 48). Down-regulation of ribosomal synthesis by high ppGpp (small σ) is well documented (49-52). Our model also expects up-regulation of AAB enzyme synthesis by ppGpp (Fig. 4b), which is supported by recent studies characterizing the transient effect of ppGpp on AAB synthesis (53).

In the second stage of our regulatory scheme, we specified the allocation of AAB enzyme synthesis towards the individual groups by introducing a set of relative allocation functions:

$$\chi_{A,\,j}(t) \equiv \eta_j(t) \cdot \chi_{A,\,tot}(t)\,. \tag{7}$$

The relative allocation functions $\eta_j(t)$ were chosen in accordance to the outcome of end-product inhibition (45, 46). A full implementation of this regulatory effect would require knowledge of the metabolite concentrations which we are not keeping track of in this work. Instead, we adopt a simple mathematical implementation as described by Pavlov and Ehrenberg (44). In this implementation (detailed in Supplementary Note 2C), feedback inhibition is determined through the present abundance of each enzyme group, $q_n(t)$. At a given time t, the AAB groups can be divided into two classes based on whether a group is growth-limiting at that time. The non-limiting group (with $q_j(t) > \lambda(t) \,/\, \lambda^*$) receives no allocation, i.e., $\eta_j(t) = 0$, while the limiting groups are allocated in proportion to their final abundances, $\phi^*_{A,\,j}$. If one orders the enzyme groups according to their relative pre-shift abundance level $q_j(0)$, i.e., $q_1(0) < q_2(0) < \cdots$, then the group-specific relative allocation imposed by end-product inhibition can be expressed as

$$\eta_j(t) = \begin{cases} 0 & j > \tilde{J}(t) \\ \phi^*_{A,\,j} \,/\, \sum_{m=1}^{\tilde{J}(t)} \phi^*_{A,\,m} & j \le \tilde{J}(t) \end{cases} \tag{8}$$

where $\tilde{J}(t)$ is the number of enzyme groups being synthesized at time t, so that the groups with $j \le \tilde{J}(t)$ are equally growth-limiting while those with $j > \tilde{J}(t)$ are not limiting.

Enzyme and growth kinetics of the two-stage model

Equations (1) through (8) completely specify our kinetic model of AA downshift. With the pre-shift and the final post-shift enzyme abundance values, $\phi_{A,\,j}(0)$ and $\phi^*_{A,\,j}$, respectively, obtained from the proteomic data (Supplementary Table 6), the model can be solved numerically to predict the quantitative time course of a long list of kinetic variables (Supplementary Table 7), including the abundances of the ribosomes, each AAB enzyme groups, as well as the overall growth dynamics, without any adjustable parameters; see Supplementary Note 3 for detailed explanation of the kinetic framework. First of all, the allocation for ribosomal synthesis $\chi_{Rb}(t)$ is predicted to be repressed right after the shift, while the total allocation for AAB enzymes $\chi_{A,\,tot}(t)$ is upregulated as shown in Fig. 4c.

The resulting changes in the abundances of these two groups of proteins, plotted as the black and green curves in Fig. 4d, capture the data (triangles) very well. The predicted allocation functions $\chi_{A,j}(t)$ for each AAB groups are shown in Fig. 4e: Right after the shift, only the Met group (orange) was synthesized since methionine was most growth limiting (based on the pre-shift reserve of the Met enzymes shown in Fig. 3c). After ~20 minutes when methionine was no longer the only growth-limiting AA, the synthesis of other AAB enzymes would turn on one after another, in a multi-step recovery process. The resulting dynamics for each enzyme group is plotted in Fig. 4f for the relative abundance $q_j(t)$ using the same color scheme. Predictions of the time courses of the abundance of each enzyme group also capture the data well (Fig. 3c-k, lines and symbols). Again, the theoretical predictions were generated without resorting to any adjustable parameters. From these solutions, we computed the onset time for each enzyme group. The results (circles in Fig. 3l) are again in good overall agreement with the observed onset time (triangles), except for the serine group as will be addressed shortly below. The onset time predicted by the model can in fact be derived analytically without resorting to numerical simulation (Supplementary Note 4), by adopting a simplifying approximation that holds the allocation for ribosome synthesis to the basal level throughout the period of AAB recovery (as justified by the data in Fig. 4d). The analytical solution highlights a key time scale setting the enzyme recovery kinetics, given by $(\lambda^* \phi_{A,tot}^{max} / \phi_{A,1}^*)^{-1}$ where λ^* and $\phi_{A,1}^*$ are the growth rate and met group abundance, respectively, in the post-shift steady state, and $\phi_{A,tot}^{max} = \chi_{A,tot}(0)$ gives the maximum allocation for AAB protein synthesis in the early phase of shift (see Supplementary Note 2D).

In addition to the kinetics of each enzyme group, our model also gave prediction on the growth kinetics itself during the shift (blue line, Fig. 5a). Although our model captured the AAB enzyme onset time very well, it predicted a growth lag (blue line) which was about only half of the 2-hr lag observed (blue circles). Together with the poor prediction of the onset time of the serine pathway (Fig. 3l), we wondered whether the problem with the overall growth kinetics was associated specifically with the delayed onset of the serine pathway. We thus repeated the AA downshift experiment by removing serine from the starting 18AA, still with the glycerol supplement. The data (red open diamonds in Fig. 5a) exhibited notably shorter lag, reducing the 2 hour lag to about 1 hour. In contrast, when we removed from the initial AA mixture of other single AAs whose pathways show late onset, the lag times changed much less (grey symbols, Extended Data Fig. 9b).

Addressing the serine problem

The origin of the “serine problem” can be traced to the common recipe for “rich medium” (33), in which the composition of serine used is 10-fold higher than that of the serine content in typical proteins (Extended Data Fig. 9a). With normal AA composition, serine is depleted well before other AAs (54, 55); the rich medium recipe is designed to suppress this problem. We reasoned that this highly unnatural serine content might have created an unintended problem for cells during AA downshift, which would normally occur without serine. Indeed, using “casamino acid” (obtained as the hydrolysis product of the protein casein (56)) as the

source of amino acid in pre-shift, we see that the growth kinetics is the same as that of '18AA-minus-ser' shift (grey circles, Fig. 5a).

To exam whether our model can capture the recovery kinetics of the downshift starting from 18AA-minus-ser, we performed additional proteomic measurements specifically for this shift. The resulting pathway abundances and the pathway onset times are plotted as red triangles in Fig. 5b-5k, again for the pathways showing at least 2-fold change in total abundance. The difference between this data set and the one analyzed earlier for shift from 18AA (blue triangles) is clearly substantial compared to difference between replicates (Extended Data Fig. 6); note the logarithmic scales for both axes. To obtain theoretical predictions for downshift starting from 18AA-minus-ser (red lines in Fig. 5a-5k), we simply replaced the pre-shift states by the pre-shift growth rate and pre-shift AAB enzyme reserves measured for the '18AA-minus-ser' shift (Supplementary Table 6). We see that consistent with the measured faster recovery in growth and AAB enzyme abundance, our model predictions quantitatively capture the faster kinetics during downshift from '18AA-minus-ser'. Calculated onset times (red circles, Fig. 5l) also capture well the observed onset times (red triangles). Importantly, this time the model also captures the overall growth curve (red line, Fig. 5a). More detailed examination into the differences in model prediction between the shift with and without serine shows that the two factors that are different between the two cases, the fractional pre-shift reserves ($q_j(0)$) and the allocation function ($\chi_{A,tot}$), both played important roles leading to notably different dynamics; see Extended Data Fig. 9c-f.

Biologically, differences between the shift with and without serine can be appreciated by examining the abundances of the major functional groups. As seen in Extended Data Fig. 4, substantial differences existed in the pre-shift proteome (t = 0), with the exclusion of serine resulting in 2-3 fold reduction in enzymes catalyzing fermentation to acetate, and a compensating 50% increase in TCA cycle enzymes along with 2-3 fold increase in enzymes for carbon catabolism and particularly glycerol uptake. While serine is known to be taken up rapidly (54, 55), the extent of its effect on the proteome is unexpected. In fact, enzymes for TCA cycles and fermentation to acetate were nearly at their respective post-steady state levels (indicated by the gold bars) when growing in AA without serine. Thus, *E. coli* appears to execute distinct programs in central carbon metabolism (CCM) based on the availability of external serine. With natural AA composition, serine would be depleted in the early phase of growth (55), and cells would be able to transition to the more respiration-leaning CCM while it still has the remaining AAs. Transition to minimal medium occurs later when AAs are depleted and CCM is already pre-adapted. In our experiment of AA downshift with serine, cells need to remodel the proteome for both AAB and CCM which took twice as long (compare blue and grey circles in Fig. 5a). From the time course of proteome dynamics in Extended Data Fig. 4, we see that for shift with serine, recovery for AAB enzymes occurred before those for CCM. This rationalizes why our model, which deals with only AAB enzyme recovery, was able to capture the AAB enzyme kinetics well (Fig. 3), but could not capture growth recovery which required also addressing remodeling CCM after the recovery of AAB enzymes.

Discussion

We investigated the allocation of the proteome of *E. coli* grown in rich or minimal media, in steady state growth and during transitions between them. The most substantial changes are the tradeoff between AAB enzymes and the translational machinery, which allows cells to achieve higher protein synthesis flux, hence growth rate, in rich media, when *de novo* AA biosynthesis is relieved (Fig. 1). However, drastically reducing the abundance of AAB enzymes causes problems when AA supply is abruptly depleted, manifested by a lag during AA downshift even when a separate carbon source is provided throughout the shift (Fig. 2).

Quantitative proteomic measurements during AA downshift revealed a hierarchy of time scales in the recovery kinetics of AAB enzymes (Fig. 3, Extended Data Fig. 5). A smoothly increasing relationship was established between the onset time and the fractional pre-shift reserve of AAB enzymes *across* pathways (Fig. 3l). The observed relationship is a manifestation of an as-needed strategy of gene regulation for AAB enzymes, where those involved in the biosynthesis of the amino acid most needed for protein synthesis, methionine, were expressed first, followed by the enzymes for the next most needed AA, arginine, etc. In this context, we recall that a related ‘just-in-time’ gene expression strategy *within* a pathway (Extended Data Fig. 10a) was proposed long ago for AA downshift (57), and was claimed as the optimal strategy for minimizing the amino acid recovery time while minimizing enzyme production cost. However, our proteomic data clearly refuted the adoption of such a strategy within AAB pathways (Extended Data Fig. 10c-f). Instead, *E. coli* adopts the just-in-time strategy *across* AAB pathways.

To quantitate recovery kinetics during AA downshift, we devised a coarse-grained model with proteome allocation specified in two stages (Fig. 4a, Supplementary Note 3). In the first stage, we extended the framework of flux-controlled regulation introduced in Erickson *et al.* (21) to AA biosynthesis, using “translational activity” to represent the collective effect of AA pools and to direct the dynamic allocation of protein synthesis flux between the AAB enzymes and ribosomal proteins. In the second stage, we allocated the synthesis of AAB enzymes into individual pathways, using the on-off strategy formulated by Pavlov & Ehrenberg (44) to capture the effect of end-product regulation (45). The resulting model has no adjustable parameters, in the sense that all model parameters (listed in Supplementary Table 6) are fixed by the growth rates and the proteomic data in the pre- and post-shift steady states. When applied to AA downshift, the model was able to quantitatively capture the onset time of most AAB enzyme groups except that for serine (Fig. 3l). However, our model failed to describe the growth transition kinetics itself. Attributing the “serine problem” to non-realistic medium composition which led to very different programs in central carbon metabolism (Extended Data Fig. 4), we repeated the analysis for AA downshift without serine, finding the model to quantitatively capture not only the enzyme recovery kinetics (Fig. 5b-5l) but also the entire growth transition kinetics (Fig. 5a). The ability of the model to capture quantitative differences in the AAB pathway recovery kinetics between the shift with and without serine (blue and red symbols in Fig. 5l) also serves as a validation of our approach, especially robustness in the construction of the allocation function for AAB enzymes (Extended Data Fig. 4).

The success of our model raises the question of whether *E. coli* cells might have evolved to minimize the recovery time, since the on-off strategy employed in our model was shown theoretically by Pavlov and Ehrenberg (PE) to give the fastest recovery kinetics within an overall proteomic resource constraint (44). Indeed, for a period after the shift when protein synthesis is allocated mostly to AAB enzymes, our model becomes a specific realization of the on-off model considered by PE (Supplementary Note 4B). However, these models only describe response to "initial conditions" imposed by the proteome set in pre-shift growth. As the initial condition affects the recovery kinetics in minimal medium, we explored the dependence of the expected recovery time on the pre-shift reserve (i.e., $q_j(0)$) for a fixed total abundance of AAB enzymes before the shift. The calculation in Supplementary Note 4D shows that a uniform pre-shift reserve would give a lag time that is less than half of the observed one; and even for randomly generated pre-shift reserves, the lag times would be in most cases shorter than the observed one. In this light, we can understand the long lag time observed as a consequence of the actual pre-shift reserves being broadly distributed over nearly two orders of magnitude (Fig. 3b), which is very far from a uniform distribution. In other words, *E. coli* arranges a very non-uniform, hierarchical distribution of pre-shift reserves, with the consequence of acquiring an exceptionally long lag time. These results suggest that even though *E. coli* uses feedback inhibition to allocate protein synthesis flux to the most limiting pathways given the pre-shift distribution, minimizing the recovery time of downshift to minimal media is not a primary concern for *E. coli* cells growing in rich media. The physiological reason for *E. coli* to acquire this broad distribution of pre-shift reserves is not understood.

In our model the allocation for ribosome synthesis ($\chi_{Rb}(t)$) was gradually turned on as AAB enzyme synthesis ($\chi_{A,tot}(t)$) was reduced (Fig. 4c), not abruptly switched on as prescribed by the on-off model (44). The portion of the proteome allocated to the ribosomes and AAB enzymes, which is the focus of this study, comprised < 30% of the total proteome (dashed line, Fig. 4b). The remainder of the proteome was allocated to such functions as carbon and AA transport, motility, as well as other housekeeping functions carrying no metabolic fluxes in the growth conditions we studied. Many of these proteins are turned on before the AAB enzymes (grey circles, Fig. 3m). If we applied the PE model to all these proteins beyond the AAB enzymes, the cells would adapt much faster. Clearly, such a strategy is not adopted by *E. coli*. Instead, *E. coli* casts its response broadly, underscoring the importance of anticipating different nutrient types when AA supplies are exhausted in the native habitat. The kinetic responses exhibited by the various protein groups reflect the interplay of their respective regulatory mechanisms which are set by a variety of physiological and ecological reasons that are mostly unknown. The coarse-grained kinetic framework described in this work can be used to quantitatively capture the regulatory functions, and from them, quantitatively predict the recovery kinetics, based merely on proteome allocation in the pre- and post-shift steady state without making assumptions on optimality.

Methods

Strain construction

The strain used in this study are either wild type *E.coli* K-12 NCM3722 strain or its derivative, see Supplementary Table 1 for details.

Growth medium

Unless stated otherwise, all the growth media used in this study were based on MOPS buffered media described in Cayley et al (58). The medium contains 40mM Mops and 4mM Tricine (adjust to pH 7.4 by NaOH), 0.1mM $FeSO_4$, 0.276 mM Na_2SO_4, 0.5 μM $CaCl_2$, 0.523 mM $MgCl_2$, and also micronutrients mixtures used in Neidhardt et al (33).

If not specified, the media used in steady-state proteomic measurements were MOPS buffered media with 50mM NaCl, 1.32mM KH_2PO_4, plus carbon source, nitrogen source and other nutrients as summarized in Supplementary Table 2. For Rich defined medium (RDM), we used kit from Teknova M2105, which was prepared based on Neidhardt *et al.* (33). Casamino acids (CAA) used was obtained from BD Bacto. The concentrations of individual amino acids are listed in Supplementary Table 4.

For most of the AA downshift experiments, the post-shift medium was MOPS buffered media with 50mM NaCl, 1.32mM KH_2PO_4, 0.4% glycerol as carbon source, and 10mM ammonia chloride as the nitrogen source. The pre-shift medium was made by the addition of 18 amino acids (all except cysteine and tyrosine) to the post-shift medium. The concentrations of those amino acids added were the same as those listed in RDM (33); see Supplementary Table 4. Cysteine was excluded because it oxidizes to cystine in aerobic growth. Tyrosine was excluded because of its poor solubility. Among the 18 amino acids added, asparagine and glutamine were prepared freshly for every experiments due to their fast degradation. In this work, some 18AA downshifts were also done with carbon sources other than glycerol, e.g., 0.2% glucose, 0.2% lactose, 0.2% xylose or 0.2% fructose; see Fig. 2c-e.

In some AA downshifts starting from fewer than 18AA (Extended Data Fig. 4b), the post-shift medium was still the same glycerol MOPS medium. The pre-shift medium (referred to as '18AA-minus-X' with X indicating the amino acid(s)) was again obtained by adding to the post-shift medium the same 18 amino acids stated above except X. The casamino acid (CAA) medium used in Fig. 5a was prepared in the same way, but with the addition of 0.2% casamino acids instead of 18AA.

In experiments using all 20 AA (Fig. 3a,b), cysteine solution was prepared and added to the medium right before inoculating cells, and tyrosine was freshly dissolved in 0.1M KOH before added to the medium. The pH of the medium with tyrosine was still around 7.4.

Cell growth and medium shift

All the steady-state measurements and medium shift experiments were performed with 5 mL of cultures grown in 20 mm diameter test tubes immersed in a 37 °C water bath

shaker shaking at 240 rpm. Shifts always started after cells reaching steady-state in pre-shift medium. To grow cells to exponential phase, we followed a standard cell growth procedure taking 3 rounds: seed culture, pre-culture and experimental culture. For seed culture, cells were inoculated to LB broth from fresh LB plate and grew for about 7 hrs. Then cells were washed with corresponding MOPS medium once and diluted to the same MOPS medium (pre-culture) with starting OD_{600} at ~10^{-3}. If inductions (e.g., 3-methylbenzyl alcohol, IPTG) were needed in these experiments, they were added to the pre-culture also. After overnight pre-culture and before the culture reaches stationary phase, cells were diluted to the same MOPS medium (experimental culture) with starting OD_{600} below 0.01. For exponential growth measurements, we let cultures grow to $OD_{600} \approx 0.5$. More than five OD measurements were taken within the range of OD_{600} = 0.05~0.5 for growth rate calculation. OD_{600} was measured by Genesys 20 spectrophotometer (Thermo Fisher), with each measurement taking 200 μL of the culture. For medium shift experiments, we let cells grow to $OD_{600} \approx 0.3$, then washed cells twice with pre-warmed post-shift medium and diluted it to $OD_{600} \approx 0.1$ in pre-warmed post-shift medium. Whole medium transition process was kept within 5 mins and the moment cells were transferred to post-shift medium was defined as “time zero”. A control shift from 18AA with glycerol to the same media was done and no lag or growth rate change was observed. We took at least five OD measurements in the pre-shift medium starting from $OD_{600} \approx 0.05$. After medium transition, we took OD measurements every 5-20 mins according to the lag time until OD_{600} reached ~0.5.

Growth rate calculation

For steady-state exponent growth rate, we simply fitted growth curve exponentially. If $R^2 < 0.999$, we didn’t take it as reliable results.

To get instantaneous growth rate, we applied Savitzky-Golay filter (59) to N $\{t_i, \ln(OD_{600,i})\}$ data set. Recall that because of medium switch, OD_{600} was not continuously at t=0. Therefore we scaled the data in post-shift region before calculating growth rate to make the first OD_{600} after shift $(t < 5\,\text{min})$ equal to the value exponentially extrapolated from pre-shift data.

The window size we used includes 3 data points. First, we fitted the first 3 data points to the 2nd polynomial and substituted t of middle data point (t_2) into fitted equation to get its slope. Then we moved the window to the right and did the same thing for the 2nd to 4th data points to get the slope at t_3. Repeating moving windows and calculating slope, we got slopes at $t_2, t_3, \ldots t_{N-1}$. We took these slopes as the “instantaneous growth rates” at $t_2, t_3, \ldots t_{N-1}$. Cells were in steady-state at t_1 and t_N according to our experimental setting, so we only plotted data points from t_2 to t_{N-1} for instantaneous growth rate plots.

Measurements of proteins using mass spectrometry

For steady-state growing cells (sample ID M1-M4, P1, P8-P10, N5-N8, O8-O10, A1-A3, A7-A9, A26-A28), we followed the cell growth protocol stated above and took samples at $OD_{600} \approx 0.4$. For each AA downshift experiment (sample ID S1-S5, A29-A39) we followed the protocol above and took one sample (S1, A29-A31) in pre-shift steady-state, at $OD_{600} \approx 0.3$. For 18AA downshifts (A32-A35), samples were taken at 15, 50, 100, 200 min after the shift started. For 18AA-minus-ser downshift (A36-A39), samples were taken at 15, 45, 75, 120mins after the shift start. We collected at least one $OD_{600} \cdot ml$ culture volume of cells for each sample by centrifuging at 13,200 RPM for 2 min.

We used quantitative mass spectrometry to characterize the abundance of *E. coli* proteomes at various growth conditions (Supplementary Table 2). The samples belong to three groups: group #1, samples M1-M4, N5-N8 and O8-O10; group #2, samples P1, P3, P8-10 and S1-5; group #3, samples A1-A3, A7-A9 and A26-A39. Samples O8-O10, P3, A1-A3 are only used for internal calibration and validation. Quantitative measurements of *E. coli* proteomes for group #1 and #2 were carried out as described previously (19). Briefly, *E. coli* cell pellets were lysed with 2% sodium deoxycholate and digested with LysC and trypsin. An iRT peptide mix (Biognosys) was added to all samples for retention time alignment. Tryptic peptides were measured in SWATH mode (64 variable windows) on a TripleTOF 5600 mass spectrometer (Sciex). The data was analyzed using OpenSWATH (as included in openMS v.2.1.0) as done in Ref. (19).

Quantitative measurements for group #3 were carried out in DIA mode on an Orbitrap Exploris 480 mass spectrometer (Thermo Fisher Scientific) and analyzed using Spectronaut and the directDIA approach (Biognosys). Details for the complete group #3 workflow are given below:

***Bacterial cell lysis and protein digestion for* group #3.—**Cells were lysed in 100 µL absolute TFA (Sigma-Aldrich; 5 min, 55°C, shaking at 1,000 rpm) and neutralized with 900 µL 2 M Tris (60). Protein concentration was determined using Bradford reagent (Sigma-Aldrich). Subsequently, 50 µg of total protein amount were reduced and alkylated (10 mM Tris(2-carboxyethyl)phosphine hydrochloride, 40 mM Chloroacetamide; 5 min, 95°C). Water-diluted samples (1:1) were subjected to proteolysis with trypsin (Roche, protein ratio 1:50, 30°C, overnight, 400 rpm). Enzymatic digestion was stopped by addition of 3% formic acid (FA). Peptide samples were desalted using self-packed desalting tips prepared in-house using five discs of Empore C18 (3M) material stacked in 200µL pipette tips. The desalting tips were conditioned with 100% acetonitrile (ACN) and 40% ACN/0.1% FA, and equilibrated with 2% ACN, 0.1% FA in HPLC grade water. Peptides were loaded, washed (2% ACN, 0.1% FA in HPLC grade water) and eluted (40% ACN, 0.1% FA in HPLC grade water). Samples were dried to completeness and re-dissolved in 30 µl 0.1% FA in HPLC grade water.13.3 µg of total peptide amount (as determined by Bradford assay) was injected into the mass spectrometer per run.

DIA-based mass spectrometric data acquisition for group #3.—Peptides were analyzed on an UltiMate 3000 (micro-flow configuration) coupled to an Orbitrap Exploris

480 mass spectrometer (Thermo Fisher Scientific). 13.3 µg of peptides were applied directly onto a commercially available Acclaim PepMap 100 C18 column (2 µm particle size, 1 mm ID × 150 mm, 100 Å pore size; Thermo Fisher Scientific), and separated using a 60 minutes linear gradient ranging from 3% to 28% solvent B (0.1% FA, 3% DMSO in ACN) in solvent A (0.1% FA, 3% DMSO in HPLC grade water) at a flow rate of 50 µl/min. The mass spectrometer was operated in data-independent acquisition (DIA) mode. MS1 full scans (360 – 1300 m/z) were acquired with a resolution of 120,000, an AGC target value of 10^6 and a maximum injection time of 50 ms. MS2 scans (200 – 1800 m/z) were acquired over a total of 40 DIA segments with widths adjusted to the precursor density (see Supplementary Table 8). The scan resolution in the Orbitrap was set to 15,000 with an AGC target value of 10^5 and a maximum injection time of 22 ms. The HCD collision energy was set to 30%.

directDIA data analysis using Spectronaut for group #3.—DIA data were analyzed with Spectronaut (v.14.2, Biognosys) using the directDIA functionality, which omits the need for an experimental spectral library. In brief, DIA raw files were loaded into Spectronaut and searched against the Uniprot-derived *Escherichia coli* (K12, MG1655) reference proteome (UP000000625, download 07.09.2021, protein entries 4438). Trypsin/P was used as digestion enzyme and up to two missed cleavages were allowed. Oxidation of methionine and acetylation of protein N-terminus were set as variable modifications, and carbamidomethylation of cysteine as fixed modification. For directDIA data extraction default settings provided by Biognosys were used. The mProphet approach was used to estimate FDR. The dataset was filtered to 0.1% FDR at peptide precursor level (q-value cutoff < 0.001). Peptide quantification was performed based on MS2 XIC peak areas, using the best N fragments per peptide (min 3, max 6).

Protein quantification and proteomics error determination.—Protein intensities were computed from the detected peptide intensities using the algorithm xTop v2.0 developed in this work. This algorithm, described and validated in Supplementary Note 1, improves over the xTop algorithm introduced in Ref. (19) by allowing estimating the uncertainty in the inferred protein abundances due to noise in the peptide precursor intensities. xTop v2.0 was applied separately on the three groups of samples using the following parameters: filter_thres=0.5; thres_xTop = 300; N_c_thres = 3; s2_min=0.01; absolute_filter_ratio = 0.1. Batch effects among different groups of samples were accounted for as follows: The relative protein abundances from groups #1 and #2 (obtained with SWATH, but in separate batches) were first harmonized by minimizing the log-ratio between the samples corresponding to glucose minimal medium and carbon-limited growth. Then, proteins from both groups were scaled so that the average protein abundances in glucose minimal medium matched the average abundances from group #3 in the same conditions. Absolute protein mass fractions were computed by calibrating the average protein abundances in samples A7, A8, A9, O10 and P3 for *E. coli* EQ353 strain to ribosome profiling data for the same strain and condition, as done in Ref. (19); protein mass fractions were computed from number fractions as done in Ref. (19). Raw proteomics data is available on the PRIDE repository (see the “Data availability” section). The resulting protein mass fractions are reported in Supplementary Table 9.

Statistics and reproducibility

Uncertainties on the absolute protein intensities were calculated by combining the errors on the xTop protein intensities and the error on ribosome profiling. Errors on the xTop protein intensities originate from the observed scatter of peptide precursors. The coefficient of variation (CV) of the ribosome profiling data from was assumed identical for all genes, and estimated as follows. For each gene, we obtained from Ref. (32) the reads in the first (L_i) and second half (R_i) of each gene i, and estimated the typical CV = 16.5 % as the average value of the empirical coefficient of variation $\sqrt{2(L_i - R_i)^2 / (L_i + R_i)^2}$ over 2870 genes with L_i and R_i>64 reads. This CV was combined with the protein- and condition-specific error from xTop to yield the error on the absolute protein fractions ϕ_i. See Supplementary Note 1 for details on both the relative and absolute error in proteomics data. The error on the total protein fraction for a group of proteins was obtained by summing in quadrature the errors for the individual proteins. When calculating the average abundance of two or more biological repeats, the error of each sample (σ_i) were taken into consideration as weights ($w_i = 1 / \sigma_i^2$).

In Figure 1a, the growth rates were measured in at least 3 biological replicates. The error bars represent the standard error on the mean.

In Figure 1b-j and Extended Data Fig. 1, the proteomic data in minimal media (black symbols) are average of two independent biological repeats (see Supplementary Table 2). Other proteomic data are from single experiments (Figure 1 green symbols, Figure 3, 5, etc.) although replicate results shown in Extended Data Fig. 4, 7 are highly similar.

In Fig. 2d, 2e, each data point is derived from a single shift experiment shown in Fig. 2c. The main experiment with glycerol as carbon source has been independently repeated more than three times (Extended Data Figure 3d).

In Figure 5a and Extended Data Figure 3, 13b, each growth curve is from a single shift experiment, among which 18AA downshift with or without ser have been repeated at least 3 times and similar lag time (less than 10% difference) were observed for biological replicates.

Modelling

The modeling approach used to capture the observed growth and proteomics data is explained in Supplementary Notes 2 through 4. Briefly, Supplementary Note 2 provides an extensive explanation of the model, relating growth and the lag time during a nutrient shift to the pre-shift abundance and the synthesis of biosynthetic enzymes, along with its assumptions; Supplementary Note 3 describes the concrete application of the model to the data; Supplementary Note 4 describes analytical expressions approximating the exact model solution, the relationship with previous model of enzyme allocation, robustness of the model with respect to noise in the input data, and whether the observed protein reserves (on which the lag time depends) are optimized for fast recovery.

Extended Data

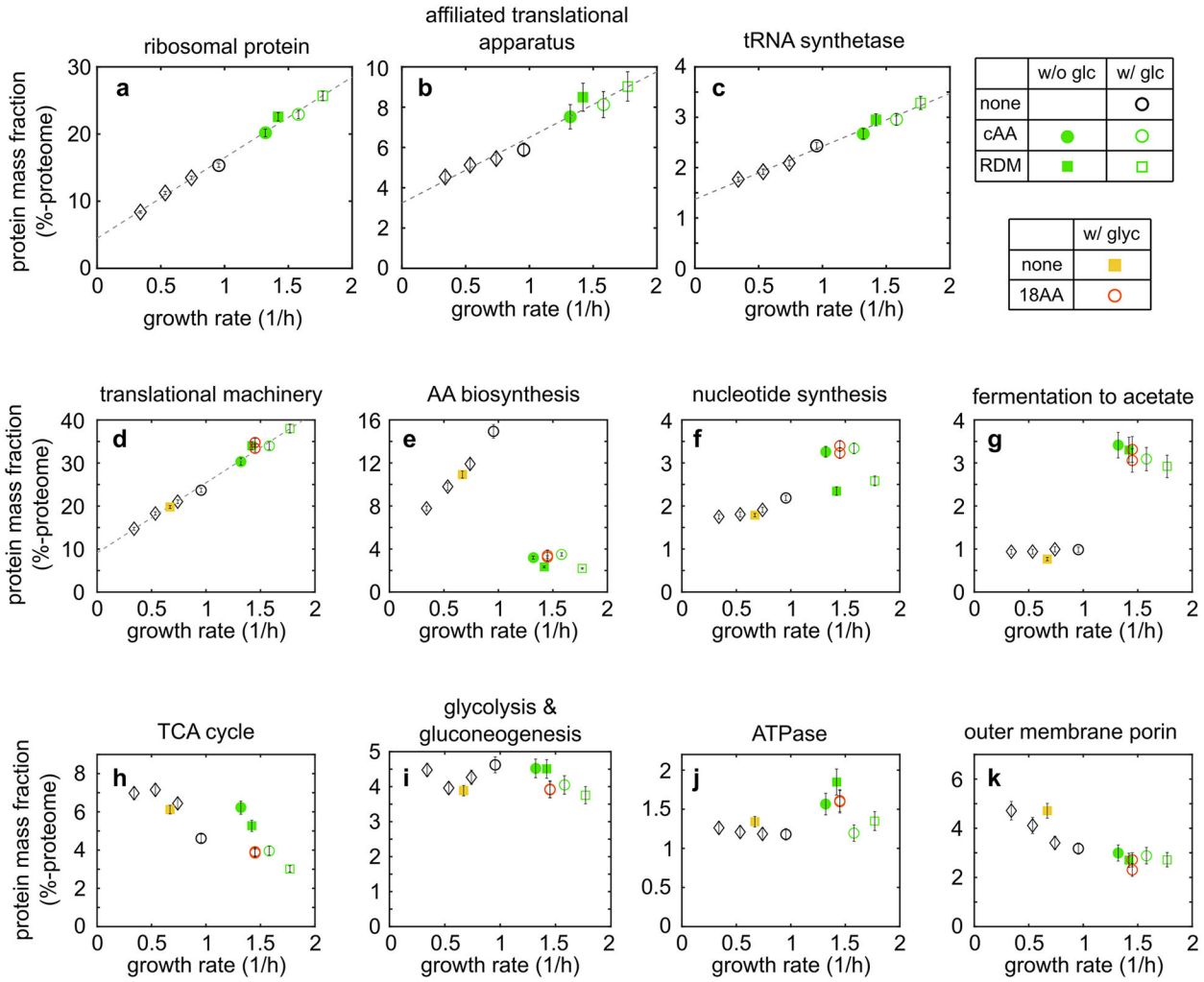

Extended Data Fig. 1.

(a-c) Breakdown of the steady state protein abundances of the translational machinery (Fig. 1) into **(a)** ribosomal proteins, **(b)** affiliated translational apparatus, and **(c)** tRNA synthetases. In all cases, the protein mass fractions are plotted against the growth rate under carbon limitations (wild type: black open circles; titratable *ptsG* mutant: black open diamonds) and four rich conditions (green symbols as shown in the legend table). The same symbols are used in Figure 1 and Extended Data Figure 2. **(d-k)** Steady state protein abundance of key metabolic enzyme groups. These panels are the same as Fig. 1c-j except with the inclusion of conditions for 18AAs with 0.4% glycerol supplement (red circles), and 0.4% glycerol as the sole carbon source (yellow squares). See Supplementary Table 2 for the details of growth conditions and Supplementary Table 3 for gene classifications. In all panels, error bars are propagated from the estimated errors for individual proteins (Methods).

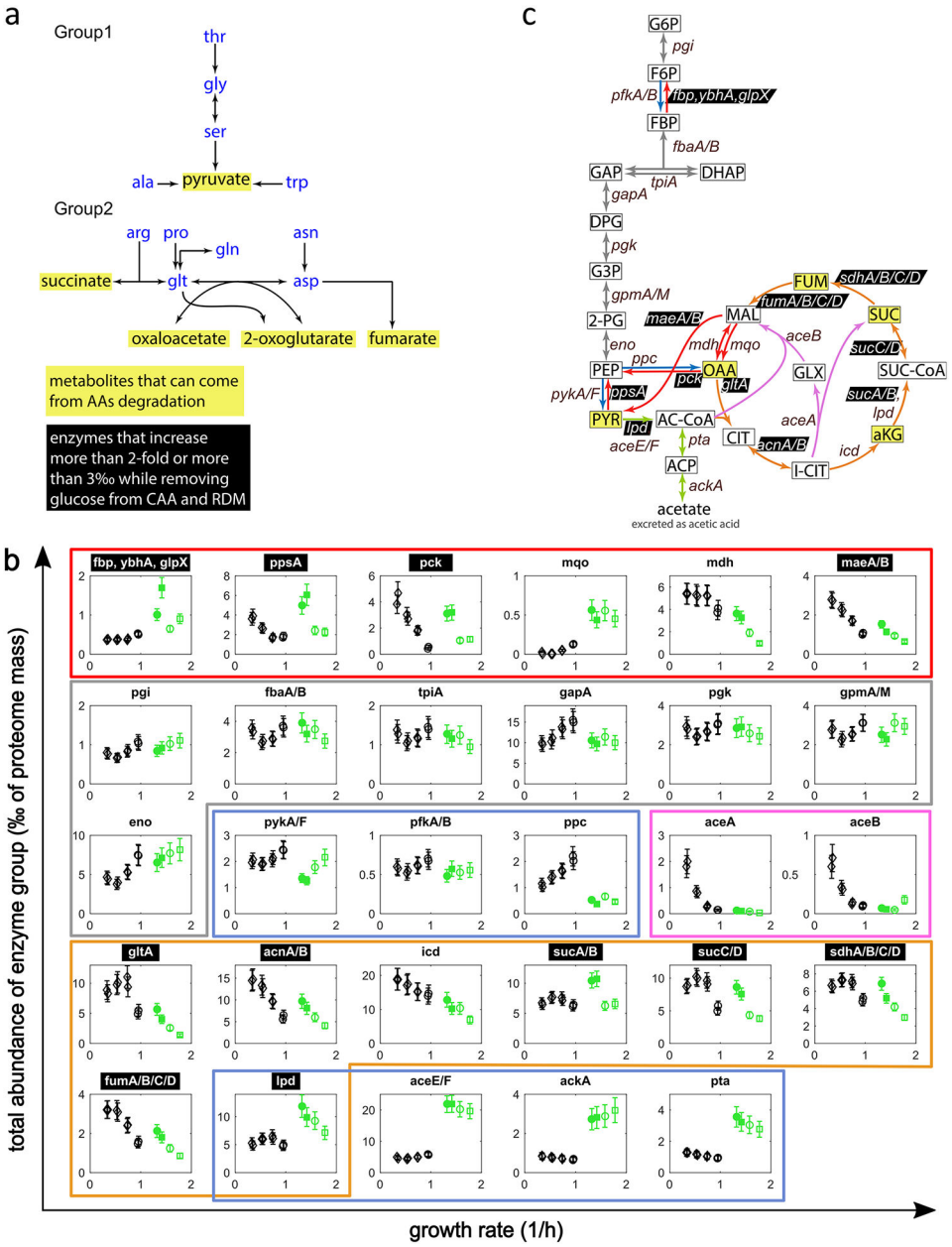

Extended Data Fig. 2.

(a) Summary of AA degradation pathways based on EcoCyc (34, 35). Five AAs (ala, ser, thr, gly, trp degrades into pyruvate, and six AAs (asp, asn, glu, gln, pro, arg) degrade into TCA intermediates. Degradation pathways are not known for the remaining 9 amino acids (leu, ile, val, met, cys, lys, his, phe, tyr). **(b)** The abundances of enzymes of Central Carbon Metabolism (CCM) in steady state growth, plotted against the growth rate. The symbols are the same as those used in Extended Data Fig. 1. The gene names shown with a black background are enzymes that increased by more than 50% or by more than 2‰ of proteome in CAA or RDM without glucose supplement compared to those with glucose supplement (i.e., increased in filled green symbols compared to open green symbols). Error bars indicate uncertainties from the protein quantification method (Methods). **(c)**

Enzymes and metabolites involved in CCM. Metabolites that can be produced from AA degradation are boxed in yellow. Reactions are represented by colored arrows with the genes encoding the corresponding enzymes written next to it in italic. The color of the arrows corresponds to the box color in panel (b), with gray indicating reversible reactions involved in both glycolysis and gluconeogenesis, red indicating gluconeogenesis only, blue indicating glycolysis only, orange indicating TCA cycle, pink indicating glyoxylate shunt, and green indicating pyruvate fermentation to acetate. The enzymes with increased abundances in rich medium without glucose supplement are clearly clustered in gluconeogenesis (red box in panel (b), 5 out of 6 enzymes) and in TCA cycle (orange box in panel b, 7 out of 8 enzymes). This suggests that in the absence of glucose supplement, the AA degradation products are funneled through CCM to supply the cell's non-AA carbon needs, e.g., energy biogenesis and the biosynthesis of lipids and cell wall components, via TCA cycle and via gluconeogenesis.

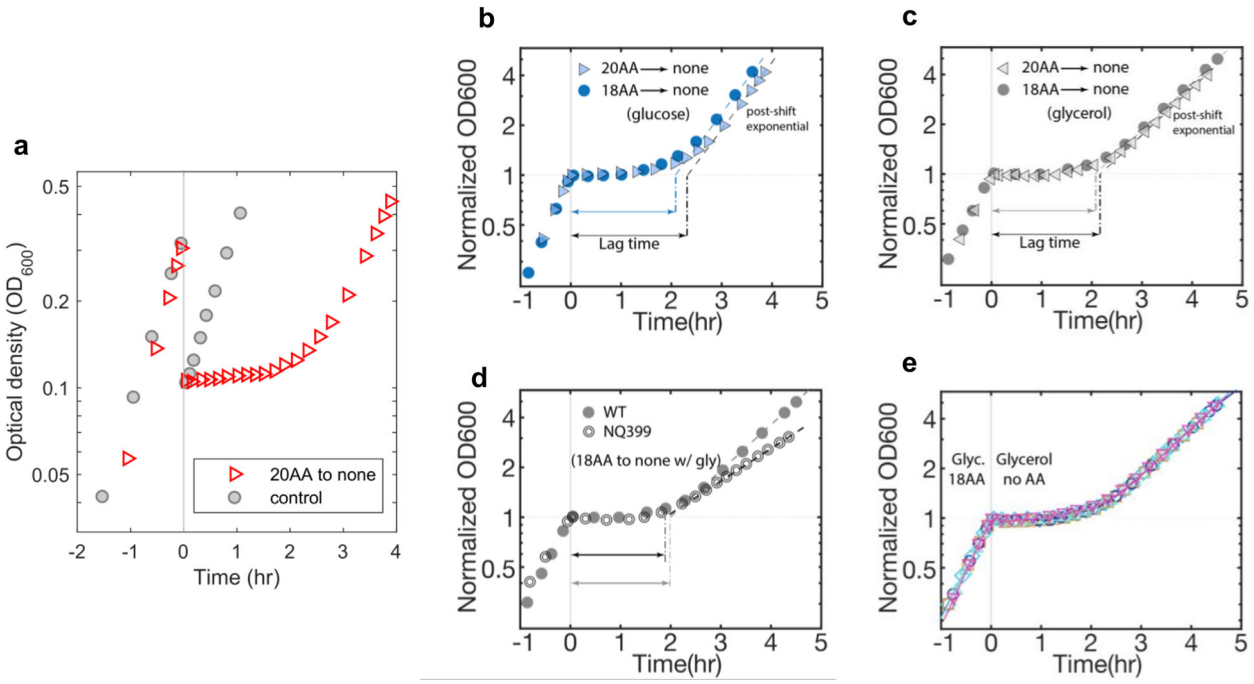

Extended Data Fig. 3.

(a) Optical density during a nutrient shift from 20AA to no AA (red triangles), supplemented with glucose, as well as a control sample (grey circles), with the same medium before and after the shift. As described in Methods, when the pre-shift culture reached $OD_{600} \sim 0.3$, we performed the shift by filtering and washing the pre-shift cell culture and re-suspending the pellets using the post-shift medium (Fig. 1b). The post-shift culture started at $OD_{600} \sim 0.1$. From this raw growth curve, we match the start of the post-shift OD_{600} to the end of the pre-shift OD_{600} to make the growth curves continuous. Then we normalized the growth curve so that the normalized OD_{600} at the start of a shift is always 1. This leads to the triangles shown in panel (b). **(b)** Comparison of AA downshift with all 20 AAs (triangles) and downshift with 18AA (excluding cysteine and tyrosine due to poor solubility and stability); see Methods and Supplementary Table 4. Both shifts are

supplemented by 0.2% glucose before and after the shift. Note the presence or absence of cysteine and tyrosine made little difference to the growth transition kinetics. **(c)** AA downshift experiments of panel **(b)** is repeated with glucose replaced by 0.4% glycerol as the carbon supplement. The growth transition is nearly the same for both 20AA-to-none and 18AA-to-none shifts. **(d)** The grey filled circles are the same as those in panel b, indicating the 18AA downshift with glycerol supplement. Open circles represent the result of the same downshift in strain NQ399 (see Supplementary Table 1), which has fully expressed glycerol uptake system (GlpFK). [1mM IPTG and 1mM 3MBA was added to the medium before and after the shift for the shift by NQ399 so that *glpFK* expression was fully induced throughout the shift (11).] The lag period did not change, indicating that the glycerol uptake system was not the bottleneck of this growth transition. **(e)** Repeatability of 18AA shift supplemented by glycerol. Symbols of different colors represent results of independent experimental runs. The CV of lag time across these runs is within 10%.

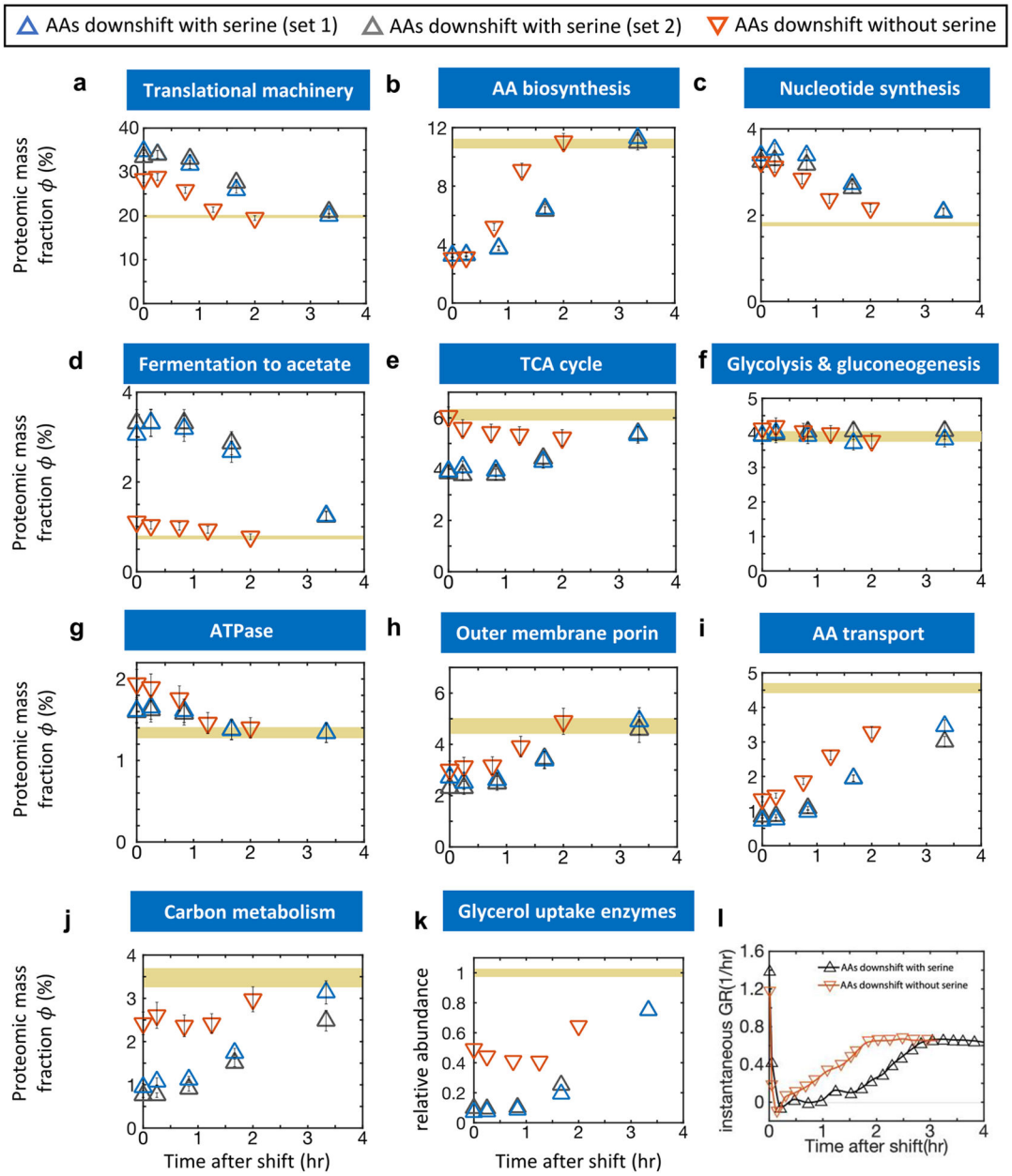

Extended Data Fig. 4.

The time dependence of the total abundance of proteins from a number of key functional groups during AA downshift with glycerol as the carbon source. The 8 functional groups in panels **(a)-(h)** are those introduced in Fig. 1; we additionally included **(i)** AA transport, **(j)** carbon catabolism, and **(k)** glycerol uptake, with the lattest added given the use of glycerol as the carbon supplement. Three sets of data are included: set 1 (blue up-triangles) and set 2 (grey up-triangles) are replicates for 18AA downshift; the third dataset indicated by the red down-triangles are for downshift starting from 18AA minus serine; see Supplementary Table 2. Raw protein abundance data for each replicate are shown in Supplementary Table 9. Membership of each functional group is shown in Supplementary Table 3. All protein abundances are reported in mass fraction (%-proteome), except for glycerol uptake enzymes

whose absolute abundance could not be fixed because these enzymes were not expressed in the reference condition where ribosome-profiling was performed (32). Data corresponding to pre-shift are shown at time 0. Error bars for all protein groups (except the glycerol uptake group) are propagated from the estimated errors for individual proteins (Methods). The horizontal gold bars indicate data for steady state growth on glycerol and no AA, which is the final post-shift stead state; the thickness of the bars indicate estimated errors. **(l)** Instantaneous growth rate (see Methods) at various time after the shift. For clarity, only one set of data is shown for 18AA downshift, as the repeatability of the growth curve is already shown in Extended Data Fig. 3e.

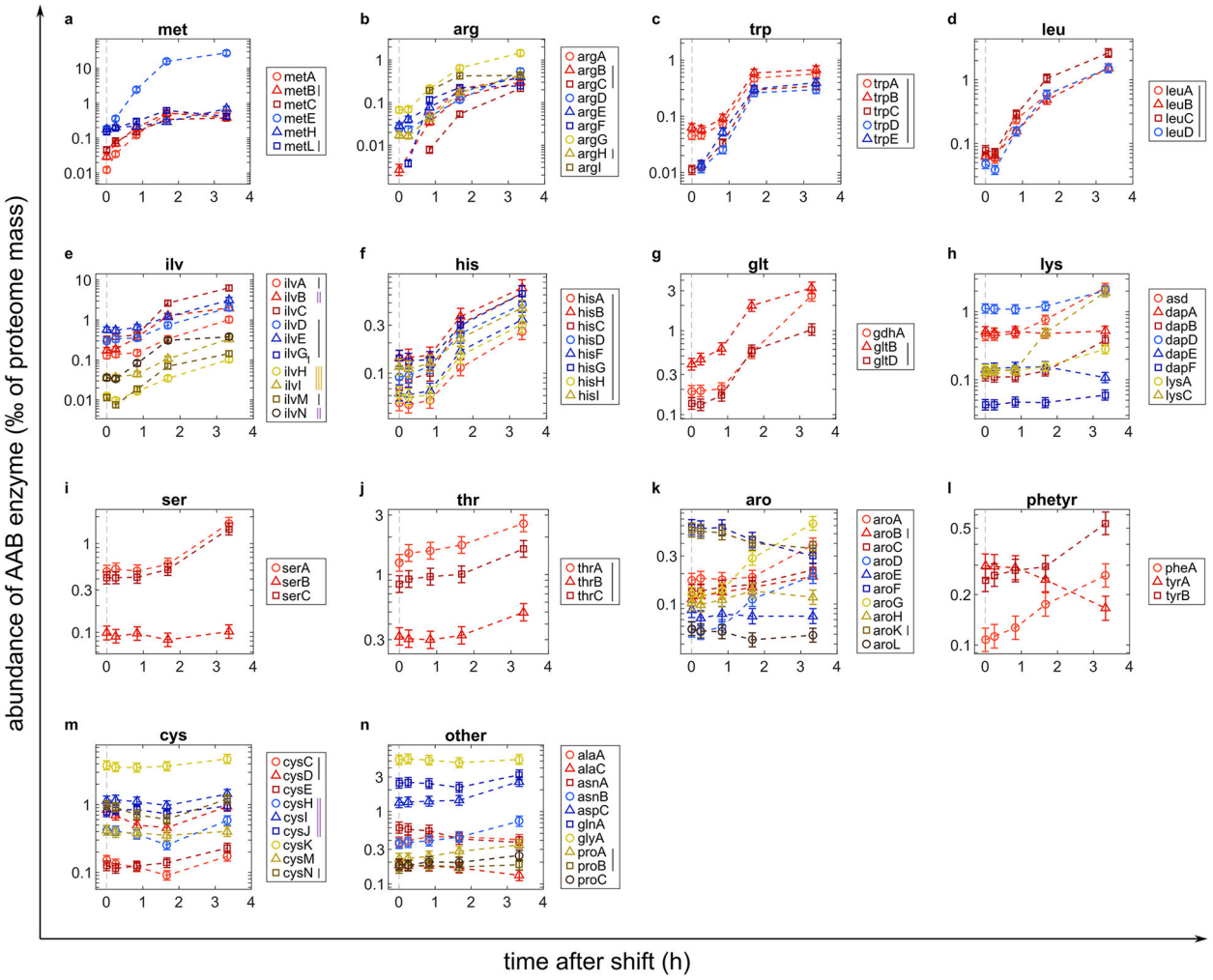

Extended Data Fig. 5.

The abundance time courses for individual AA biosynthesis enzymes during ‘18AA-to-none’ shift (set 1) supplemented by glycerol. The enzymes in the same pathway are plotted in the same plot. Error bars represent standard errors obtained using the xTop protein quantification method (Methods). In each panel, the lines in the legend box next to the gene name indicates the operon structure. The same line style means the genes belong to the same operon. E.g., for panel **(m)**, *cysC* and *cysN* are in one operon, *cysHIJ* are in another operon,

while *cysD*, *cysE*, *cysK*, *cysM* are by themselves. The genes in different groups don't share operons except *serC-aroA* and *aroF-tyrA*. In each panel, the similar color of the recovery curves indicating similar kinetic behavior. E.g., in **(i)**, SerA and SerC (both in red) have similar kinetics, while SerB (in blue) is different. Similar kinetic behavior in panels **c-d,f,j** are all attributable to the operon structure. Similar kinetic behaviors are also seen in other panel where the genes are not in the same operons. More specifically, in the met group **(a)**, changes in the abundance of MetE dominated the entire group. In the arg group **(b)**, most enzymes showed large increase between 15 min and 50 min after the shift, except ArgA, ArgD, ArgH. The total abundance of this group was mainly determined by the abundance of ArgG and ArgI. In the ilv group **(e)**, several enzymes (e.g. ilvC, ilvN) exhibited moderate increase in the first 50 min, while the rest increased only after 50 min. Since IlvC is much more abundant than the other enzymes, the group kinetics was largely determined by this enzyme alone. In the lys group **(h)**, three enzymes (DapA, DapE, DapF) were approximately constant throughout the shift. The rest started increasing after 50 min, most of which showed only small increases during the shift, except for LysC, with a big jump between 50 min and 100 mins. But since LysC is not the most abundant enzyme in the lys group, it did not significantly affect the group kinetics itself. In the aro group **(k)**, most of the enzymes stayed constant or dropped during the shift. Three enzymes clearly increased during the shift, among which AroG was the most abundant. In the phetyr group **(l)**, decrease in TyrA could likely be attributed to the fact that tyrosine was not provided in the pre-shift medium, so that TyrA was fully expressed before the shift and was then shutoff (with abundance decreasing due to dilution) during the growth recovery phase.

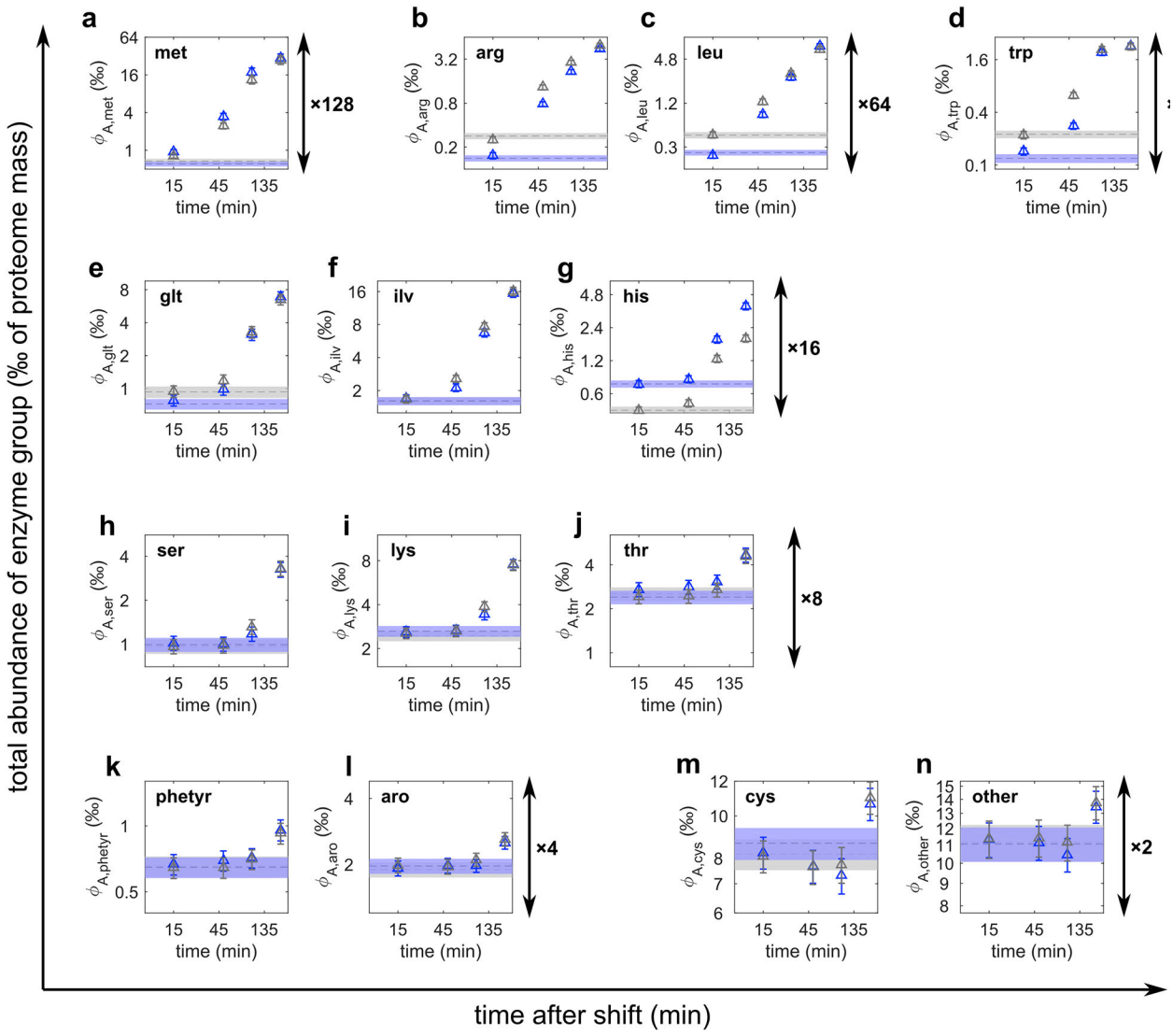

Extended Data Fig. 6.

Panels **a-i** are the same as Fig. 3c-k, but showing both replicates of 18AA downshift (blue and grey triangles). Also shown are a number of AAB groups whose total enzyme abundances changed by < 2-fold (panels **j-n**). Colored bands indicate the abundances in the pre-shift conditions, with the dashed lines indicating the measured value and the width indicating the standard error. In all cases, errors on protein groups are propagated from the estimated errors for individual proteins (see Methods).

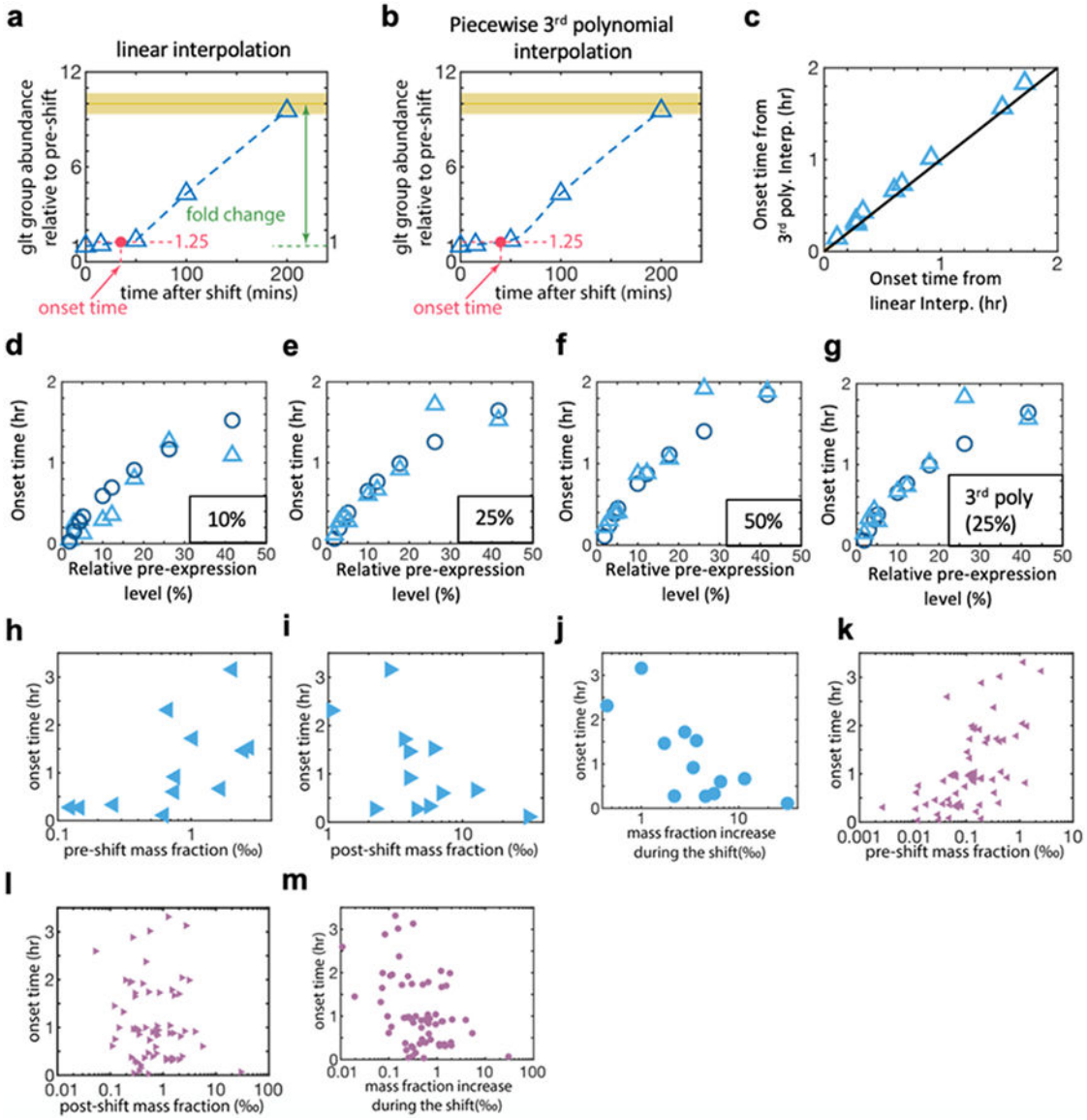

Extended Data Fig. 7.

(a) The total abundance of the glt group relative to the pre-shift total abundance is plotted at different times after the shift (same data as Fig. 3f. Between the measured data points, we used linear interpolation (blue dashed lines) to connect the data points. The green arrow shows the fold-change in enzyme abundance in post-shift steady-state (yellow bar) from the pre-shift level for the glt pathway. The red arrow indicates the onset time, defined as the time when the enzyme abundance exceeds the pre-shift value by 25%. **(b)** Same as panel a, but with a piecewise 3rd degree polynomial interpolation of the time course of the enzyme abundance. **(c)** The onset times obtained from the linear and 3rd degree polynomial interpolation are hardly different. **(d)-(g)** The onset time obtained from various definition for each AAB pathway is plotted against the inverse of fold change in the total protein abundance of that pathway (triangles). Panel (e) is the same as that shown in Fig. 3l. Panel (d) and (f) show the same but with onset threshold defined as 10% and 50% from the

initial value, respectively. Panel g is with 3rd degree polynomial interpolation. Circles are model predictions of onset time. **(h-j)** show plots of the onset time (defined as in panel a) against the pre-shift, the post-shift abundances and the increase from pre- to post- shift for individual AAB enzymes, respectively. The Pearson's correlation coefficient between the onset time and the pre-shift abundance (or the log of abundance) is 0.56 (or 0.61). The Pearson's correlation coefficient between the onset time and the post-shift abundance (or the log of abundance) is -0.45 (or -0.56). The Pearson's correlation coefficient between the onset time and the increase abundance from pre- to post-shift (or the log of abundance) is -0.50 (or -0.75). Due to the definition of the onset time in **(a)**, the enzymes with fold change less than 1.25 or undetected in the pre-shift condition do not have defined onset times, and are thus excluded in the plots. **(k-m)** show plots of the onset time with the pre-shift, the post-shift abundance and the increase abundance from pre- to post- shift for all enzymes of each pathway, respectively.

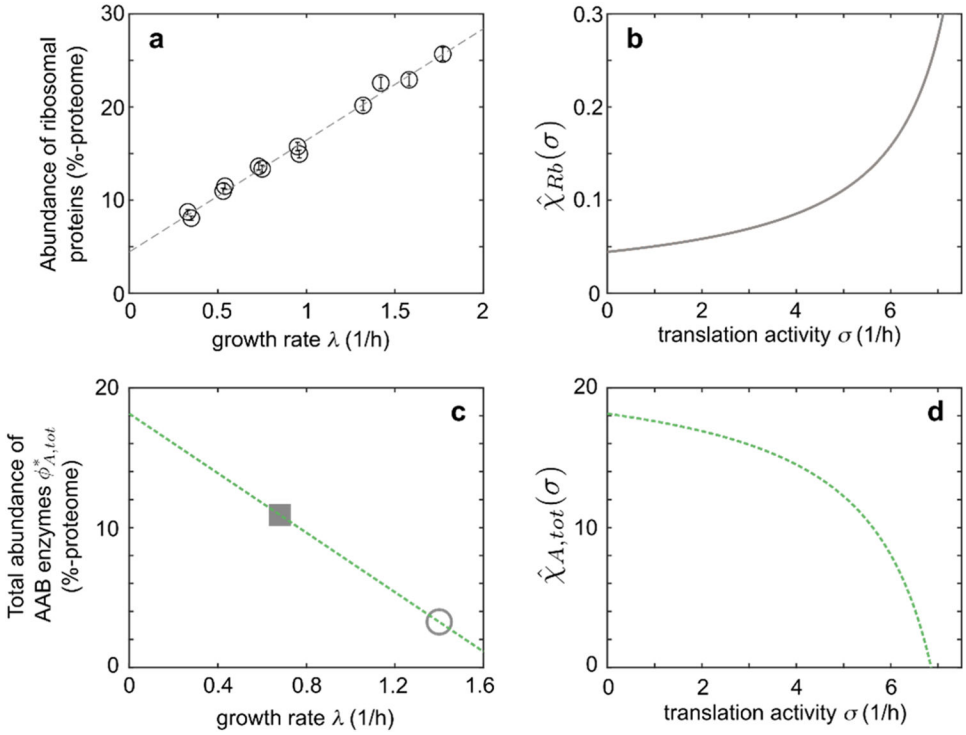

Extended Data Fig. 8.

(a) shows the abundance ϕ^*_{Rb} of ribosomal proteins at different growth rate (λ^*) for cultures growing exponentially in different nutrient sources. [Same data as that shown in Extended Data Fig. 1a; errors are propagated from the errors for individual ribosomal proteins (Methods).] The data is well-captured by a linear fit (dashed line), i.e., $\phi^*_{Rb} = \phi_{Rb,0} + \lambda^* / \gamma$, with $\phi_{Rb,0} = 4.45\,\%$ and inverse slope $\gamma = 8.35\,h^{-1}$. In steady state, we have $\chi^*_{Rb} \equiv \phi^*_{Rb}$, obtained by setting $\frac{d}{dt}\phi_{Rb} = 0$ in Eq. (2) of the main text. Using the definition of σ in Eq. (4) of the main text,

$$\sigma^* = \frac{\lambda^*}{\phi_{Rb}^*} = \frac{\lambda^*}{\phi_{Rb,0} + \lambda^* / \gamma} \tag{F8.1}$$

we can invert Eq. (F8.1) to obtain $\lambda^*(\sigma^*)$, and obtain the regulatory function as

$$\hat{\chi}_{Rb}(\sigma) = \chi_{Rb}^*(\sigma) = \phi_{Rb}^*(\lambda^*(\sigma)) = \frac{\phi_{Rb,0}}{1 - \sigma / \gamma}. \tag{F8.2}$$

The function obtained is sketched as the gray line in panel **(b)** and in Fig. 4b. **(c)** The form of the regulatory function for the total AAB enzymes, $\hat{\chi}_{A,tot}(\sigma)$, is derived similarly to that of $\hat{\chi}_{Rb}(\sigma)$. We start with the steady state abundance $\phi_{A,tot}^*$ of the AAB enzymes in different growth conditions: the value in the pre-shift steady-state is indicated in figure by the open circle, and that of the post-shift steady-state is indicated by the filled square. We connect these two points by a straight line (green dash line) to yield the relation $\phi_{A,tot}^* = \phi_{A,tot}^{max} - \alpha_A \lambda^*$ with $\phi_{A,tot}^{max} = 18.1\,\%$ and $\alpha_A = 0.11\,h$. Using Eq. (F8.1) to relate λ^* to σ^*, we obtain

$$\hat{\chi}_{A,tot}(\sigma) = \phi_{A,tot}^*(\lambda^*(\sigma)) = \phi_{A,tot}^{max} - \alpha_A \cdot \sigma \hat{\chi}_{Rb}(\sigma), \tag{F8.3}$$

where $\hat{\chi}_{Rb}(\sigma)$ is given by Eq. (F8.2). The resulting function is plotted in panel **(b)**. This form shows that when the translational activity σ is low (reflecting limitation by the shortage of AAs), AAB enzymes are expected to be up-regulated. This is consistent with our qualitative expectation that due to the global regulation of ppGpp, cells allocate more protein synthesis to AAB enzymes after AA downshift. Quantitatively, the expression for $\hat{\chi}_{A,tot}(\sigma)$ arise from the hypothesized linear relation between $\phi_{A,tot}^*$ and λ^* shown in **(a)**.

The hypothesized linear relation shown in **(a)** is difficult to measure directly. Our hypothesis of the negative linear relation in **(a)** is based on previous characterization of protein allocation under various modes of metabolic limitations (11, 15): For exponentially growing cells with growth rate limited by the influx of carbon substrate in minimal medium, it was shown that the abundance of carbon catabolic enzymes increased linearly with decreasing growth rate, a distinct phenotype referred to as the “C-line”. Similarly, under internal bottleneck in AA biosynthesis, the abundances of various AAB enzymes increased linearly with decreasing growth rate, referred to as the “A-line”. The linear response depicted in panel (a) is in fact a form of the A-line characterized in Ref. (11), a response to limitation in AA fluxes consumed by the ribosomes. Thus, the linear form described by Eq. (F8.3) is well motivated, and its two parameters can be fixed by the abundances of AAB enzymes in the two steady state conditions, before and after the shift.

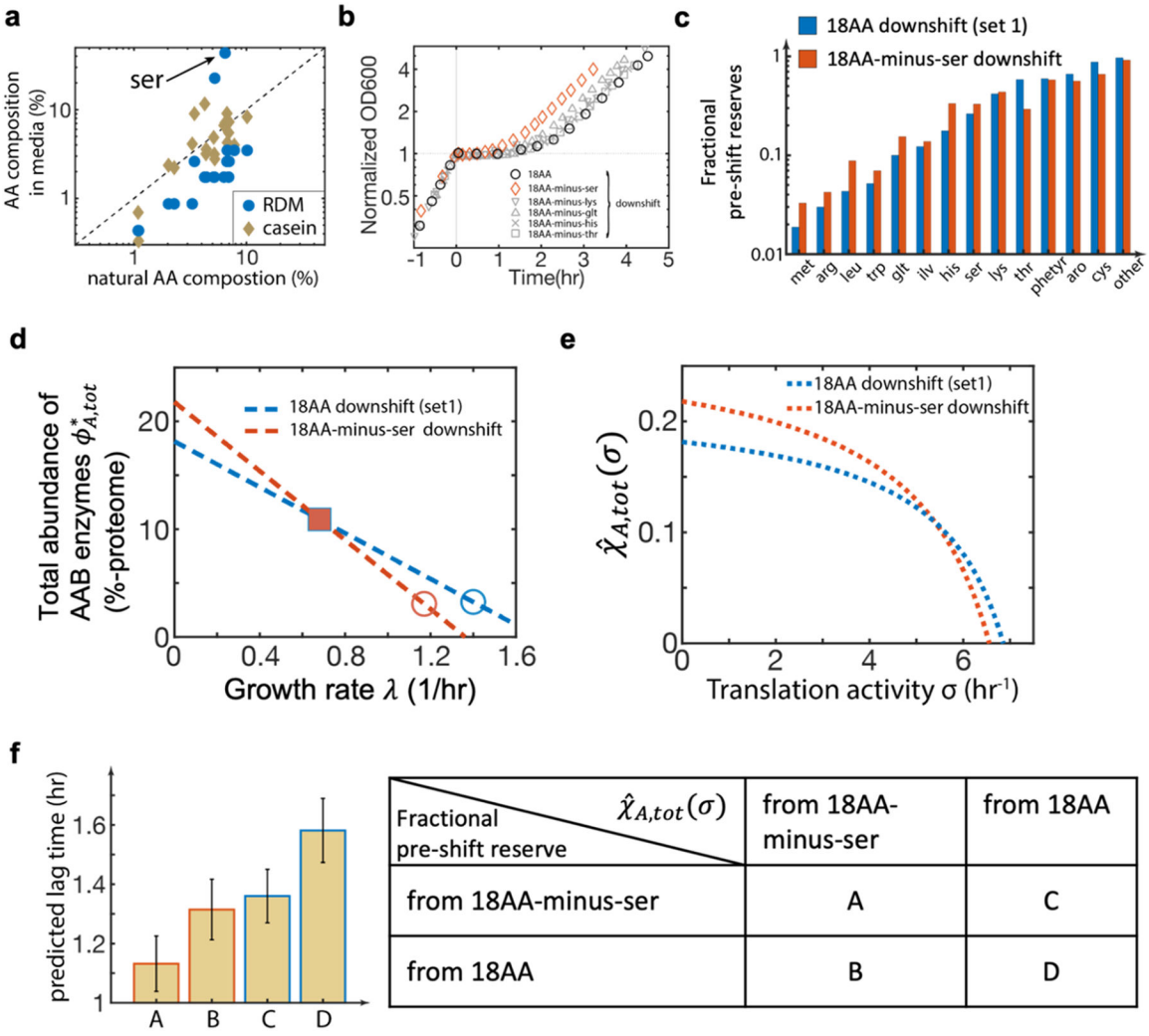

Fractional pre-shift reserve \ $\hat{\chi}_{A,tot}(\sigma)$	from 18AA-minus-ser	from 18AA
from 18AA-minus-ser	A	C
from 18AA	B	D

Extended Data Fig. 9.

Our model did not quantitatively capture the growth kinetics of 18AA downshift as seen in Fig. 5a (compare blue line and blue circles) despite its success in predicting the recovery kinetics of most AAB pathways. The discrepancy between the observed and predicted growth curves likely has to do with the behavior of the serine pathway, whose recovery kinetics was also poorly predicted (Fig. 3j). **(a)** The common recipe of AA composition for the "rich medium" we used (RDM) contained >10-fold higher serine than the natural AA composition in proteins (blue circles, with arrow pointing to serine); see Ref. (33) for recipe for RDM and Ref. (56) for the composition of the protein casein (brown diamond) from which casamino acids is derived, with the latter similar to the natural AA frequency across proteins (61), plotted as the x-coordinate. (**b**) Growth curve for '18AA-minus-ser' downshift (red diamond) shows a significantly shorter lag than 18AA downshift (black circles). In comparison, if the shift starts from withholding another aa instead of ser, e.g., thr, lys, his, glu, chosen because the onset time of these enzyme groups are the closest to that of the ser group (Extended Data Fig. 7), the corresponding growth curves (grey symbols) exhibited similar lag as the 18AA shift. This comparison shows that there is something special for AA downshift involving serine.

In the main text, we showed that our model was able to capture accurately the shift if serine is excluded, i.e., the 18AA-minus-ser downshift. Below, we provide a more detailed analysis of factors that lead to different predictions for the model with and without serine. We note that differences in model predictions with and without serine are completely dictated by the two different pre-shift states. It can be attributed to two aspects: First, fractional pre-shift reserves of the AAB groups, $q_j(0)$, are somewhat different as shown in panel (**c**). Second, different form of the allocation function $\chi_{A,tot}$ as shown in panel (**e**), constructed based on the relationship between total AAB enzyme abundance and growth rates (panel d). To analyze the contribution of each aspect, we mixed and matched the model input as shown in the table in panel (**f**) and calculated the lag time in each case. In each case, the height of the bar representing the average of n=1000 model runs obtained by randomly generating the input data (growth rates and protein abundances, assumed normally distributed) using the uncertainties reported in Supplementary Table 6; error bars represent the standard deviation of the simulated data. The lag difference predicted for the shift with and without serine (combinations A and D) is well beyond the uncertainty range. Although $\chi_{A,tot}$ is constructed from only two data points, its form is reliable in predicting the lag time of different shift. Furthermore, since the lag duration of the combinations B and C are in the middle of the lag time for A and D, we conclude that the difference in model predictions for the two shifts received similar contributions from $\chi_{A,tot}$ and from fractional pre-shift reserves $q_j(0)$.

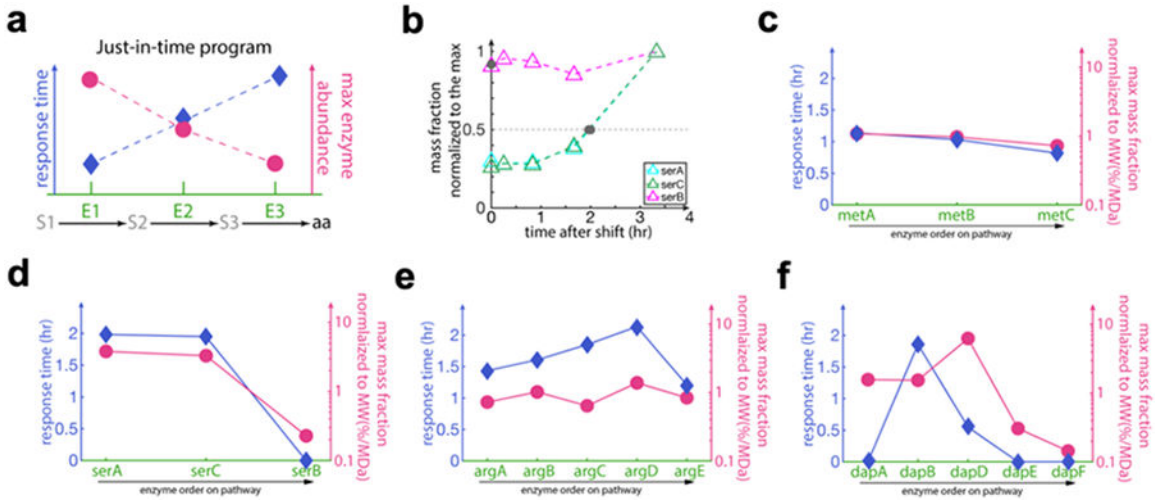

Extended Data Fig. 10.

(a) The 'just-in-time' program of enzyme recovery kinetics proposed by Zaslaver *et al* (57) states that during AA downshift, the response time of an enzyme in a linear pathway is shorter if it is located towards the beginning of the pathway (as indicated by the blue symbols), while the maximum abundance is higher towards the beginning of the pathway (as indicated by the red symbols). **(b)** Examples of response time calculated based on the proteomic measurements of SerA, SerB, SerC (Extended Data Fig. 6i). Between the measured data points, we used linear interpolation (gray dash lines) to connect the data points. The x-coordinates of the solid dots represent the corresponding response times, defined as the time when the enzyme abundance reaches 50% of the maximum during

the shift according to Zaslaver *et al.* (57). For enzyme abundance exceeding 50% at the beginning of the shift (as in the case of SerB), we took the response time to be zero. **(c)-(f)** The observed response times and maximum enzyme abundances for 4 linear segments of the AAB pathways are plotted in the order of enzyme locations for met in panel **(c)**, ser in panel **(d)**, arg in panel **(e)**, lys in panel **(f)**. Neither the response time nor the maximum abundance exhibited the predicted trends shown in **(a)** for any of the 4 pathways. While some of the differences may arise from the fact that the study of Zaslaver *et al.* limited a single amino acid while our study limited 18 amino acids, we note that the derivation of the 'just-in-time' program done in Zaslaver *et al.* assumed that the synthesis of an enzyme in a pathway depended only on the pool of its substrates. This assumption ignored the crucial condition that all amino acids, including the one being limited, are needed in order to synthesize the enzymes. Analysis based on this assumption may well be applicable to the generic onset of a metabolic pathway where it was first proposed (62), but hard to justify for the onset of an AAB pathways where the end-product of the pathway is a limiting factor of AAB enzyme synthesis.

Supplementary Material

Refer to Web version on PubMed Central for supplementary material.

Acknowledgments

We are grateful to Xiongfeng Dai, Vadim Patsalo, and Rohan Balakrishnan for helpful discussions and technical assistance during the course of this work. We also thank Oyarzun Diego for comments and suggestions. This research is supported by the NSF Grant MCB 1818384 and NIH Grant R01GM109069 through TH. CL and MA have been supported by EPIC-XS funded by the Horizon 2020 program of the European Union (project number 823839). RA acknowledges the support of the European Research Council (Proteomics4D: AdvG grant 670821 and Proteomics v3.0: AdvG-233226).

Data availability

The data underlying the figures are presented in Source Data. Other data are available from the corresponding authors upon request.

All mass spectrometric raw data files as well as the data analysis output files have been deposited to the ProteomeXchange Consortium (http://proteomecentral.proteomexchange.org) via the PRIDE partner repository with the dataset identifier PXD035278. The *E. coli* spectral library used for DIA/SWATH data analysis has been published previously (19) and is available via SWATHAtlas: http://www.peptideatlas.org/PASS/PASS01421.

Code availability

The code used to compute protein intensities (xTop v2) is available on https://gitlab.com/mm87/xtop. The code used to model the AA downshift growth kinetics based on the mathematical model presented in the main text is available on https://gitlab.com/ch47/model-of-aa-downshift.

Reference

1. Yao CK, Muir JG, Gibson PR, Review article: insights into colonic protein fermentation, its modulation and potential health implications. Aliment. Pharmacol. Ther 43, 181–196 (2016). [PubMed: 26527169]
2. Oliphant K, Allen-Vercoe E, Macronutrient metabolism by the human gut microbiome: major fermentation by-products and their impact on host health. Microbiome 2019 71 7, 1–15 (2019).
3. Kellerman AM, Dittmar T, Kothawala DN, Tranvik LJ, Chemodiversity of dissolved organic matter in lakes driven by climate and hydrology. Nat. Commun 2014 51 5, 1–8 (2014).
4. Sniatala B, Kurniawan TA, Sobotka D, Makinia J, Othman MHD, Macro-nutrients recovery from liquid waste as a sustainable resource for production of recovered mineral fertilizer: Uncovering alternative options to sustain global food security cost-effectively. Sci. Total Environ 856, 159283 (2023). [PubMed: 36208738]
5. Koch AL, The adaptive responses of Escherichia coli to a feast and famine existence. Adv. Microb. Physiol 6, 147–217 (1971). [PubMed: 4950180]
6. Mori M, Schink S, Erickson DW, Gerland U, Hwa T, Quantifying the benefit of a proteome reserve in fluctuating environments. Nat. Commun 8, 1–8 (2017). [PubMed: 28232747]
7. Schaechter M, MaalØe O, Kjeldgaard NO, Dependency on Medium and Temperature of Cell Size and Chemical Composition during Balanced Growth of Salmonella typhimurium. Microbiology 19, 592–606 (1958).
8. Neidhardt FC, Magasanik B, Studies on the role of ribonucleic acid in the growth of bacteria. Biochim. Biophys. Acta 42, 99–116 (1960). [PubMed: 13728193]
9. Maaløe O, Goldberger RF, Biological regulation and development. Biol. Regul. Dev 1, 487–542 (1979).
10. Scott M, Gunderson CW, Mateescu EM, Zhang Z, Hwa T, Interdependence of cell growth and gene expression: origins and consequences. Science 330, 1099–1102 (2010). [PubMed: 21097934]
11. You C, et al. , Coordination of bacterial proteome with metabolism by cyclic AMP signalling. Nature 500, 301–306 (2013). [PubMed: 23925119]
12. Liebermeister W, et al. , Visual account of protein investment in cellular functions. Proc. Natl. Acad. Sci. U. S. A 111, 8488–8493 (2014). [PubMed: 24889604]
13. Li Z, Nimtz M, Rinas U, The metabolic potential of Escherichia coli BL21 in defined and rich medium. Microb. Cell Fact 13, 1–17 (2014). [PubMed: 24387764]
14. Scott M, Hwa T, Shaping bacterial gene expression by physiological and proteome allocation constraints. Nat. Rev. Microbiol 2022, 1–16 (2022).
15. Hui S, et al. , Quantitative proteomic analysis reveals a simple strategy of global resource allocation in bacteria. Mol. Syst. Biol 11, 784 (2015). [PubMed: 25678603]
16. Peebo K, et al. , Proteome reallocation in Escherichia coli with increasing specific growth rate. Mol. BioSyst 11, 1184–1193 (2015). [PubMed: 25712329]
17. Schmidt A, et al. , The quantitative and condition-dependent Escherichia coli proteome. Nat. Biotechnol 34, 104–110 (2016). [PubMed: 26641532]
18. Caglar MU, et al. , The E. coli molecular phenotype under different growth conditions. Sci. Rep 7, 45303 (2017). [PubMed: 28417974]
19. Mori M, et al. , From coarse to fine: the absolute Escherichia coli proteome under diverse growth conditions. Mol. Syst. Biol 17, e9536 (2021). [PubMed: 34032011]
20. Wick LM, Quadroni M, Egli T, Short- and long-term changes in proteome composition and kinetic properties in a culture of Escherichia coli during transition from glucose-excess to glucose-limited growth conditions in continuous culture and vice versa. Environ. Microbiol 3, 588–599 (2001). [PubMed: 11683869]
21. Erickson DW, et al. , A global resource allocation strategy governs growth transition kinetics of Escherichia coli. Nature 551, 119–123 (2017). [PubMed: 29072300]
22. Wang X, Xia K, Yang X, Tang C, Growth strategy of microbes on mixed carbon sources. Nat. Commun 10, 1279 (2019). [PubMed: 30894528]

23. Basan M, et al. , A universal trade-off between growth and lag in fluctuating environments. Nature 584, 470–474 (2020). [PubMed: 32669712]
24. Molenaar D, van Berlo R, de Ridder D, Teusink B, Shifts in growth strategies reflect tradeoffs in cellular economics. Mol. Syst. Biol 5, 323 (2009). [PubMed: 19888218]
25. Weiße AY, Oyarzún DA, Danos V, Swain PS, Mechanistic links between cellular trade-offs, gene expression, and growth. Proc. Natl. Acad. Sci 112, E1038–E1047 (2015). [PubMed: 25695966]
26. Dourado H, Lercher MJ, An analytical theory of balanced cellular growth. Nat. Commun 2020 111 11, 1–14 (2020).
27. Bruggeman FJ, Planqué R, Molenaar D, Teusink B, Searching for principles of microbial physiology. FEMS Microbiol. Rev 44, 821–844 (2020). [PubMed: 33099619]
28. de Groot DH, Hulshof J, Teusink B, Bruggeman FJ, Planqué R, Elementary Growth Modes provide a molecular description of cellular self-fabrication. PLOS Comput. Biol 16, e1007559 (2020). [PubMed: 31986156]
29. Roy A, Goberman D, Pugatch R, A unifying autocatalytic network-based framework for bacterial growth laws. Proc. Natl. Acad. Sci 118, e2107829118 (2021). [PubMed: 34389683]
30. Gillet LC, et al. , Targeted data extraction of the MS/MS spectra generated by data-independent acquisition: a new concept for consistent and accurate proteome analysis. Mol. Cell. Proteomics 11, O111.016717 (2012).
31. Ludwig C, et al. , Data-independent acquisition-based SWATH-MS for quantitative proteomics: a tutorial. Mol. Syst. Biol 14, e8126 (2018). [PubMed: 30104418]
32. Li G-W, Burkhardt D, Gross C, Weissman JS, Quantifying absolute protein synthesis rates reveals principles underlying allocation of cellular resources. Cell 157, 624–635 (2014). [PubMed: 24766808]
33. Neidhardt FC, Bloch PL, Smith DF, Culture Medium for Enterobacteria. J. Bacteriol 119, 736–747 (1974). [PubMed: 4604283]
34. Keseler IM, et al. , The EcoCyc database: reflecting new knowledge about Escherichia coli K-12. Nucleic Acids Res. 45, D543–D550 (2017). [PubMed: 27899573]
35. Karp PD, et al., "The EcoCyc Database" in EcoSal Plus: Cellular and Molecular Biology of E. Coli, Salmonella, and the Enterobacteriaceae, (ASM Press, 2018), pp. 200–400.
36. Dai X, et al. , Reduction of translating ribosomes enables Escherichia coli to maintain elongation rates during slow growth. Nat. Microbiol 2, 16231 (2016). [PubMed: 27941827]
37. Maaløe O, "Regulation of the Protein-Synthesizing Machinery---Ribosomes, tRNA, Factors, and So On" in Biological Regulation and Development: Gene Expression, Goldberger RF, Ed. (Springer US, 1979), pp. 487–542.
38. Bremer H, Dennis PP, Modulation of Chemical Composition and Other Parameters of the Cell at Different Exponential Growth Rates. EcoSal Plus 3 (2008).
39. Milo R, What is the total number of protein molecules per cell volume? A call to rethink some published values. Bioessays 35, 1050–1055 (2013). [PubMed: 24114984]
40. Oldewurtel ER, Kitahara Y, van Teeffelen S, Robust surface-to-mass coupling and turgor-dependent cell width determine bacterial dry-mass density. Proc. Natl. Acad. Sci 118, e2021416118 (2021). [PubMed: 34341116]
41. Balakrishnan R, et al. , Principles of gene regulation quantitatively connect DNA to RNA and proteins in bacteria. bioRxiv, 2021.05.24.445329 (2021).
42. Björkeroth J, et al. , Proteome reallocation from amino acid biosynthesis to ribosomes enables yeast to grow faster in rich media. Proc. Natl. Acad. Sci 117, 21804–21812 (2020). [PubMed: 32817546]
43. Okano H, Hermsen R, Kochanowski K, Hwa T, Regulation underlying hierarchical and simultaneous utilization of carbon substrates by flux sensors in Escherichia coli. Nat. Microbiol 5, 206–215 (2020). [PubMed: 31819215]
44. Pavlov MY, Ehrenberg M, Optimal control of gene expression for fast proteome adaptation to environmental change. Proc. Natl. Acad. Sci. U. S. A 110, 20527–20532 (2013). [PubMed: 24297927]

45. Smith CA, Physiology of the Bacterial Cell. A Molecular Approach. Biochem. Educ 20, 124–125 (1992).
46. Elf J, Berg OG, Ehrenberg M, Comparison of repressor and transcriptional attenuator systems for control of amino acid biosynthetic operons. J. Mol. Biol 313, 941–954 (2001). [PubMed: 11700051]
47. Wu C, et al. , Cellular perception of growth rate and the mechanistic origin of bacterial growth law. Proc. Natl. Acad. Sci 119, e2201585119 (2022). [PubMed: 35544692]
48. Hwa T, The physics of living matter space, time and information : the proceedings of the 27th Solvay Conference On Physics, Brussels, Belgium, 19-21 October 2017, Gross D, Sevrin A, Shraiman B, Eds. (World Scientific, 2020).
49. Potrykus K, Cashel M, (p)ppGpp: Still Magical? Annu. Rev. Microbiol 62, 35–51 (2008). [PubMed: 18454629]
50. Lemke JJ, et al. , Direct regulation of Escherichia coli ribosomal protein promoters by the transcription factors ppGpp and DksA. Proc. Natl. Acad. Sci 108, 5712–5717 (2011). [PubMed: 21402902]
51. Scott M, Klumpp S, Mateescu EM, Hwa T, Emergence of robust growth laws from optimal regulation of ribosome synthesis. Mol. Syst. Biol 10, 747 (2014). [PubMed: 25149558]
52. Hauryliuk V, Atkinson GC, Murakami KS, Tenson T, Gerdes K, Recent functional insights into the role of (p)ppGpp in bacterial physiology. Nat. Rev. Microbiol 13, 298–309 (2015). [PubMed: 25853779]
53. Sanchez-Vazquez P, Dewey CN, Kitten N, Ross W, Gourse RL, Genome-wide effects on Escherichia coli transcription from ppGpp binding to its two sites on RNA polymerase. Proc. Natl. Acad. Sci 116, 8310–8319 (2019). [PubMed: 30971496]
54. Yang Y, et al. , Relation between chemotaxis and consumption of amino acids in bacteria. Mol. Microbiol 96, 1272–1282 (2015). [PubMed: 25807888]
55. Zampieri M, Hörl M, Hotz F, Müller NF, Sauer U, Regulatory mechanisms underlying coordination of amino acid and glucose catabolism in Escherichia coli. Nat. Commun 10, 3354 (2019). [PubMed: 31350417]
56. Gordon WG, Semmett WF, Cable RS, Morris M, Amino Acid Composition of α-Casein and β-Casein2. J. Am. Chem. Soc 71, 3293–3297 (1949).
57. Zaslaver A, et al. , Just-in-time transcription program in metabolic pathways. Nat. Genet 36, 486–491 (2004). [PubMed: 15107854]
58. Cayley S, Lewis BA, Guttman HJ, Record MT, Characterization of the cytoplasm of Escherichia coli K-12 as a function of external osmolarity: Implications for protein-DNA interactions in vivo. J. Mol. Biol 222, 281–300 (1991). [PubMed: 1960728]
59. Steinier J, Termonia Y, Deltour J, Smoothing and differentiation of data by simplified least square procedure. Anal. Chem 44, 1906–1909 (1972). [PubMed: 22324618]
60. Doellinger J, Schneider A, Hoeller M, Lasch P, Sample Preparation by Easy Extraction and Digestion (SPEED) - A Universal, Rapid, and Detergent-free Protocol for Proteomics Based on Acid Extraction * . Mol. Cell. Proteomics 19, 209–222 (2020). [PubMed: 31754045]
61. Gilis D, Massar S, Cerf NJ, Rooman M, Optimality of the genetic code with respect to protein stability and amino-acid frequencies. Genome Biol. 2, research0049.1 (2001). [PubMed: 11737948]
62. Klipp E, Heinrich R, Holzhütter H-G, Prediction of temporal gene expression. Eur. J. Biochem 269, 5406–5413 (2002). [PubMed: 12423338]

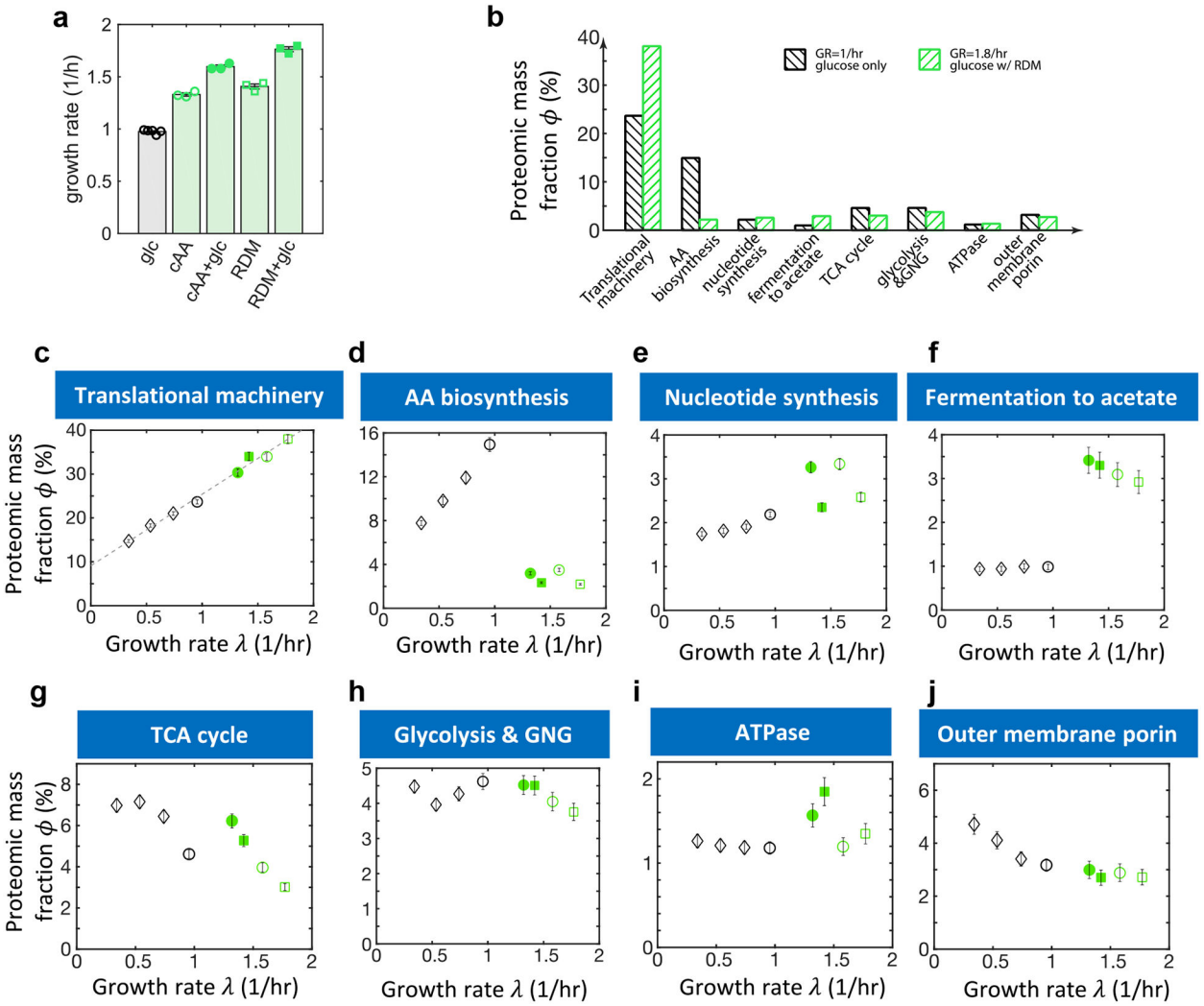

Figure 1. Steady-state protein abundances.

(a) The steady-state growth rate of *E. coli* K-12 NCM3722 cells are shown for various minimal and rich media used in this study (Supplementary Table 2): minimal medium with glucose as the sole carbon source, casamino acid (CAA) with glucose and without glucose, and rich-defined medium (RDM) with glucose and without glucose. The CVs of the growth rates are no more than 3% based on at least 3 replicates. Bars indicate average growth rates; error bars indicate standard error on the mean. **(b)** Proteomic allocation comparison between glucose minimal media (black bars) and RDM with glucose (green bars). The mass fraction changes in translational machinery and AAB enzymes are dominant compared to others. **(c)-(j)** Total abundance of proteins in various protein groups, as obtained from mass spectrometry and reported as fraction of total protein mass ("proteome fraction"), is plotted against the growth rate of each culture. Classification of proteins into groups are specified in Supplementary Table 3 according to Refs. (34, 35). In addition to NCM3722 cells in the 5 conditions described in panel (a), the plots also show (as open diamonds) the results for slower-growing mutants with limited expression of glucose uptake protein PtsG (36, 43) to help visualize the trend; see Supplementary Table 1 for strain details. The error bars

on protein abundances, indicating a standard deviation, reflect the scatter in the peptide precursors detected in the mass-spectrometry data (via xTop v2.0; see Supplementary Note 1) and a basal noise level originating from the uncertainty in the absolute scale of protein abundance (see Methods).

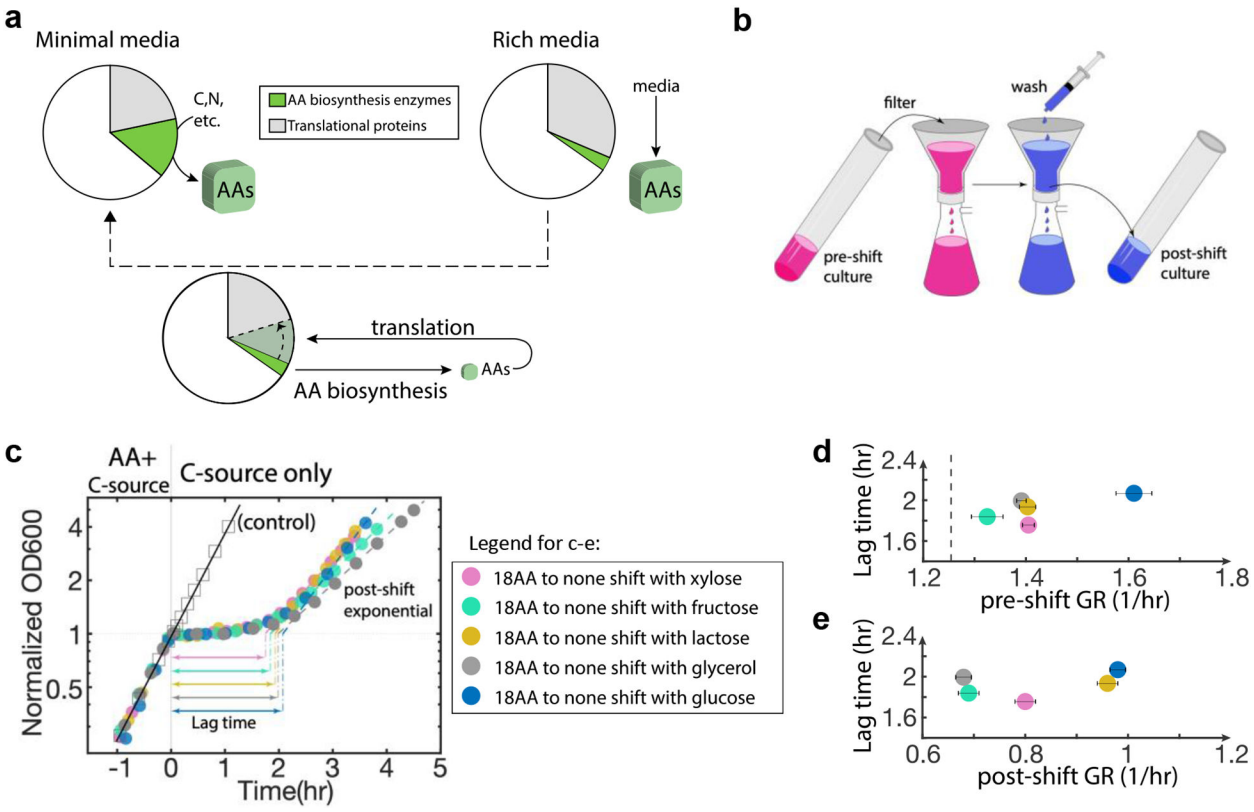

Figure 2. AA downshift with various carbon supplement.

(a) Remodeling of the proteome needed during AA downshift. Pie charts shows the steady-state proteomic allocation in glucose minimal media and in CAA supplemented with glucose. Grey sector represents translational proteins, green sector represents AA biosynthesis (AAB) enzymes, and the white sector represents other proteins. In minimal media, cells need to synthesize AAs using AAB enzymes, which are expressed at low levels in rich media. When the environment suddenly changes from rich media to minimal media (dash line), cells suffer from the shortage of both AAs and AAB enzymes. Limited AAB enzymes provide limited AA fluxes, which limit the synthesis of all proteins including the AAB enzymes. **(b)** shows a schematic diagram of the medium shift performed in this study, with the entire duration of the shift taking < 5 min. **(c)** Growth curves for downshift from 18AA (Supplementary Table 4) for WT strain, while maintaining one of the carbon sources shown in the legend throughout the shift. Time 0 is the downshift time; see Extended Data Fig 3a. “Lag time” is defined by extrapolating the exponential growth of post-shift steady state to the OD of the culture at the time of shift. The open squares show the results for control experiment from 18AA with glycerol to the same medium, demonstrating that the filter-wash process in **(b)** does not affect cell growth. **(d)-(e)** Scatter plots of lag times against pre-shift and post-shift steady-state growth rates for the shifts shown in **(c)** using the same color scheme. The vertical dash line in panel **(d)** shows the growth rate of the culture on 18AA without additional carbon source. The horizontal error bars in **(d)** and **(e)** shows 95% confidence interval, coming from exponential fitting of growth curves. Typical variation from biological repeats were within 5% for growth rate measurements and within

10% for lag time measurements (see Extended Data Fig. 3e for repeatability of the growth curves).

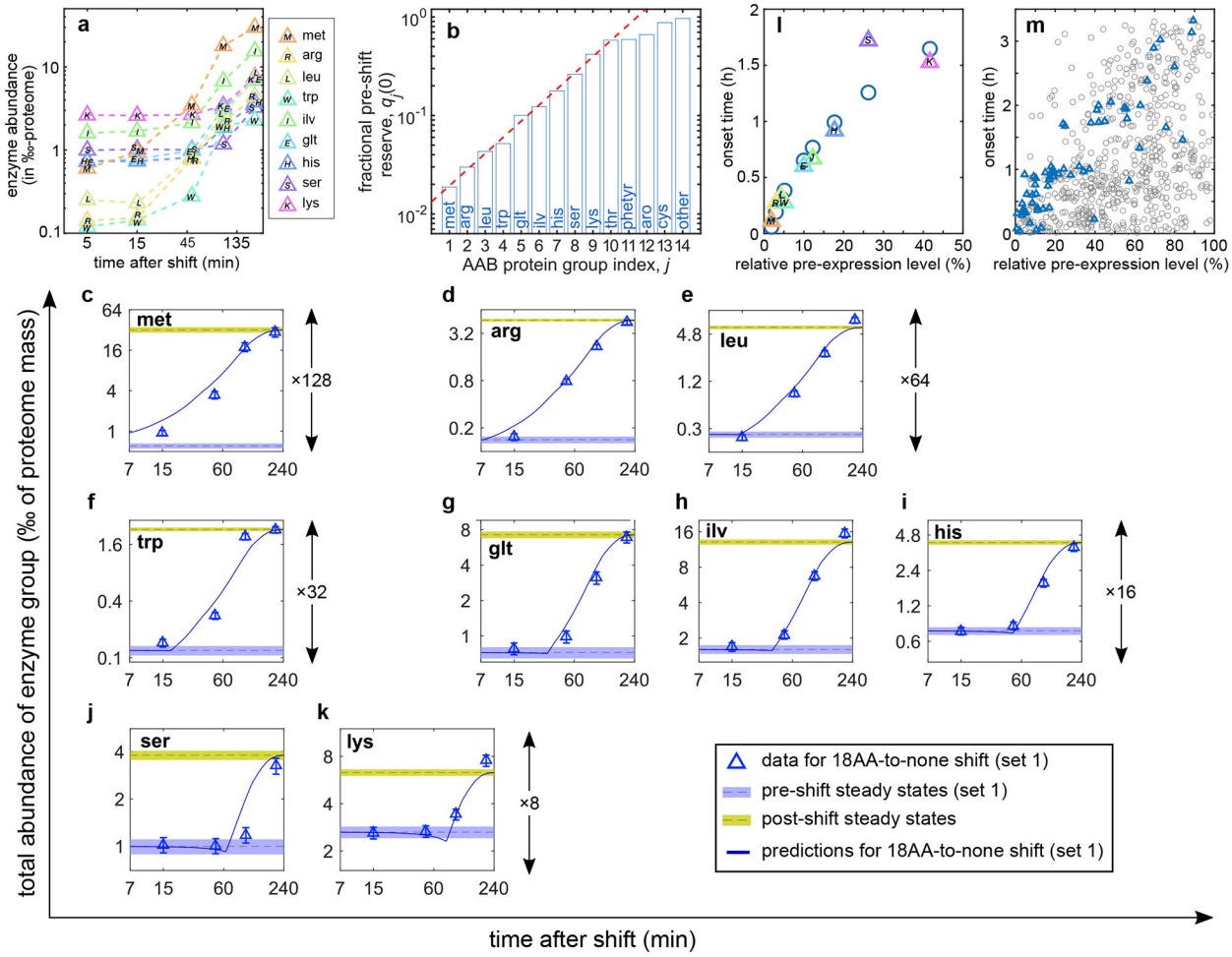

Figure 3. Enzyme recovery kinetics for individual AAB groups.

(a) AAB enzymes are sorted into different groups according to the pathways they are in (Supplementary Table 3). The total enzyme abundance of each group that has changed at least 2-fold, expressed in term of the fraction of total protein mass, is plotted at time t=15 min, 50 min, 100 min and 200 min after the amino acid down-shift. See Extended Data Fig. 5 for the abundances of individual enzymes in each group. The data are plotted in log scales in both axes. **(b)** Pre-shift abundance level relative to final post-shift level (the reciprocal of the fold change), referred to as the "pre-shift reserve" $q_j(0)$. The reserves for the first 10 AAB groups show an approximate exponential trend, with $q_j(0) \propto e^{0.38 \cdot j}$ (red dashed line). **(c-k)** Enzyme abundance of each of the pathways in panel (a). The total abundances before the shift are shown as blue bars, while the total abundances in the post-shift steady state are shown as the gold bars. Error bars and the width of the horizontal bars represent the estimated standard errors from our proteomics pipeline (see Methods). Solid lines represent the model predictions (see text). **(l)** Onset time of each enzyme group, as defined in Extended Data Fig. 7a, against the pre-shift reserve. Circles indicate the onset time predicted from the model. Clearly, the onset time observed for the ser group is well off from the predicted value; this will be investigated below. **(m)** Same as the previous panel,

but for all the up-regulated genes during the shift (grey circles), in which AAB genes are shown as blue triangles.

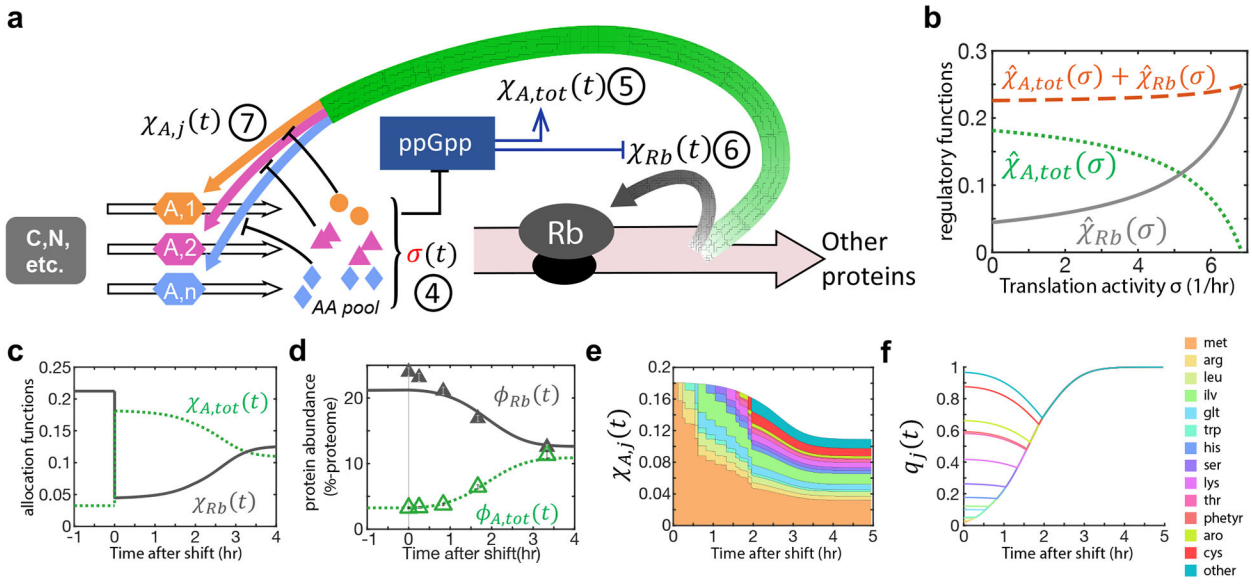

Figure 4. Model of dynamic proteome allocation for AA downshift.

(a) Upon AA removal, cells synthesize AAs *de novo* using AA biosynthesis (AAB) enzymes, indicated as A.1, A.2, etc. The AAs synthesized (indicated as circles, triangles, and diamonds) are consumed by ribosomes (Rb) for protein synthesis. Limited AA synthesis fluxes lead to limited AA pools and reduced ribosome activity, denoted by $\sigma(t)$ and defined mathematically by Eq. (4). $\sigma(t)$ serves here as a "signal" reflecting the AA pools, representing the (inverse of) the alarmone ppGpp (14, 21). It controls the allocation of protein synthesis flux to AAB enzymes and ribosomal proteins, indicated by the thick green and grey arrows, respectively. The latter are described by the allocation functions, $\chi_{A,tot}(t)$ and $\chi_{Rb}(t)$, respectively, and set by the regulatory functions $\hat{\chi}_{Rb}(\sigma)$ and $\hat{\chi}_{A,tot}(\sigma)$ according to Eqs. (5) and (6). The protein synthesis flux directed to AAB enzymes is further allocated to the enzymes of each pathway by the pathway-specific allocation function $\chi_{A,j}(t)$ specified in Supplementary Note 2D. **(b)** shows the forms of the regulatory functions $\hat{\chi}_{Rb}(\sigma)$ and $\hat{\chi}_{A,tot}(\sigma)$, solid gray and dotted green lines, respectively, constructed through the relation between the steady-state growth rate and the abundances of the corresponding protein sectors as detailed in Extended Data Fig. 8. **(c)** Time courses of the allocation functions $\chi_{Rb}(t)$ (solid grey line) and $\chi_{A,tot}(t)$ (dotted green line), obtained by solving the complete model defined by Eqs. (1)-(8). **(d)** Time courses of ribosomal protein abundance (grey) and total AAB enzyme abundance (green) for model predictions (lines) and experimental data (triangles). Error bars are obtained combining the errors estimate from individual proteins in each group (Methods). **(e)** Time courses of the predicted regulatory functions $\chi_{A,j}(t)$ (stacked) for each AAB group. The areas with different colors represent the allocation functions for the different AAB groups as described by the legend on the right. The top curve represent the time course of $\chi_{A,tot}$ since it is the sum of $\chi_{A,j}$. **(f)** Time courses of the relative abundance $q_j(t) = \phi_{A,j}(t) / \phi^*_{A,j}$ for each AAB group j. Eventually all the $q_j(t)$ reach one, indicating cells reach the final steady-state expression levels.

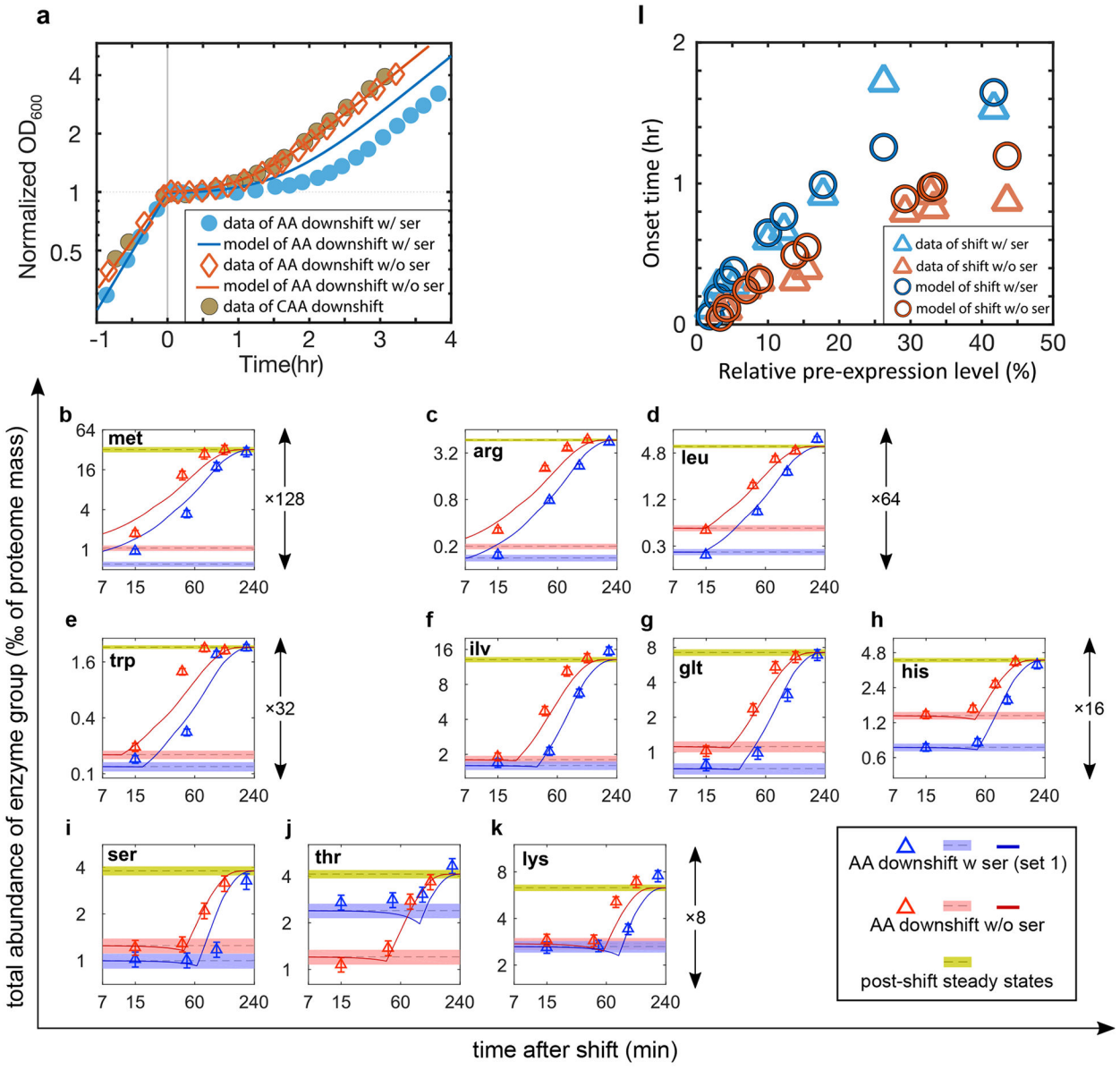

Figure 5. Data and model for AA downshift without serine.

(a) The model for AA downshift (blue line) predicted significantly shorter lag than the data (filled blue circles). The growth curve for AA downshift without serine (open red diamonds) is similar to that for downshift starting with casamino acid (CAA, filled grey circles), with significantly shorter lag and is accurately captured by the corresponding model (red line). **(b)-(k)** Recovery kinetics for total enzyme abundance of each AAB for AA downshift without serine (red triangles). Blue triangles are the data for the same pathways during downshift with serine (same as those shown in Fig. 3c-k). Only pathways with at least 2-fold change in total abundance are shown. Blue and red bars indicate the abundances in the pre-shift steady state, while the gold bars indicate the abundances in the post-shift steady state (same for the two shifts). Error bars and the width of the colored bars indicate the standard errors propagated from the errors of individual proteins (Methods). Red lines

are the recovery kinetics predicted for the shift without serine, based on the same model as that used for shift with serine (Fig. 3) but using the pre-shift growth rate and proteome data for steady-state growth in AA without serine; see Extended Data Fig. 9 for details. Blue lines are model predictions for shift with serine (same as in Fig. 3c-k). **(l)** Comparison of observed and predicted onset time for each pathway (red triangles and circles) for the shift without serine, plotted against the corresponding fractional pre-shift reserves. Blue triangles and circles are the same plot for the shift with serine (same as those in Fig. 3l).